



# Diffusion and partition coefficients of minor and trace elements in magnetite as a function of oxygen fugacity at 1150 °C

R. H. Sievwright<sup>1,2</sup> · H. St. C. O'Neill<sup>3</sup> · J. Tolley<sup>3</sup> · J. J. Wilkinson<sup>1,2</sup> · A. J. Berry<sup>2,3</sup>

Received: 14 January 2020 / Accepted: 25 March 2020 / Published online: 10 April 2020  
© The Author(s) 2020

## Abstract

Lattice diffusion coefficients and partition coefficients have been determined for Li, Mg, Al, Sc, Ti, Cr, V, Mn, Co, Ni, Cu, Zn, Ga, Y, Zr, Nb, Mo, In, Lu, Hf, Ta and U in single crystals of natural magnetite as a function of oxygen fugacity ( $fO_2$ ) at 1150 °C and 1 bar by equilibration with a synthetic silicate melt reservoir. Most experiments were run for twelve hours, which was sufficient to generate diffusion profiles from 25 to > 1000  $\mu\text{m}$  in length. The results were checked at one condition with two additional experiments at 66.9 and 161 h. The profiles were analysed using scanning laser-ablation inductively-coupled-plasma mass-spectrometry. Diffusion coefficients ( $D$ ) were calculated by fitting data from individual element diffusion profiles to the conventional diffusion equation for one-dimensional diffusion into a semi-infinite slab with constant composition maintained in the melt at the interface. Equilibrium magnetite/melt partition coefficients are given by the ratio of the interface concentrations to those in the melt. Plots of  $\log D$  as a function of  $\log fO_2$  produce V-shaped trends for all the investigated elements, representing two different mechanisms of diffusion that depend on  $(fO_2)^{-2/3}$  and  $(fO_2)^{2/3}$ . Diffusion coefficients at a given  $fO_2$  generally increase in the order: Cr < Mo  $\approx$  Ta < V < Ti < Al < Hf  $\approx$  Nb < Sc  $\approx$  Zr  $\approx$  Ga < In < Lu  $\approx$  Y < Ni < U  $\approx$  Zn < Mn  $\approx$  Mg < Co < Li < Cu. Thus, Cu contents of magnetites are most susceptible to diffusive reequilibration, whereas the original content of Cr should be best preserved.

**Keywords** Magnetite · Diffusion · Trace element partitioning · Oxygen fugacity · Petrogenetic indicator

## Introduction

Trace element concentrations in magnetite vary considerably between different deposit types (Dare et al. 2012; Nadoll et al. 2014) and can, therefore, be used as a tool for fingerprinting mineralisation styles and interpreting primary conditions of crystallisation. Variations in trace element

chemistry of igneous magnetite may be due in part to differences in parameters such as temperature, bulk melt composition, oxygen fugacity ( $fO_2$ ) and pressure, which dictate equilibrium element partitioning behaviour. However, partitioning of trace elements can also occur at disequilibrium. Diffusion (disequilibrium) processes can act to modify the original magnetite chemistry, particularly in igneous systems. Thus, to utilise magnetite as a petrogenetic tool, it is important to understand the transport properties of elements within the mineral so that the likelihood and timescales necessary for the trace element chemistry to be influenced by disequilibrium element partitioning can be assessed.

Magnetite (ideally  $\text{Fe}^{2+}\text{Fe}^{3+}_2\text{O}_4$ ) is a common mineral in igneous and metamorphic rocks and has been studied extensively with regard to diffusion. A large volume of early work focused on oxidation kinetics (e.g. Dieckmann 1982). At low temperature,  $\text{Fe}_3\text{O}_4$  has an inverse spinel structure, in which both  $\text{Fe}^{2+}$  and  $\text{Fe}^{3+}$  occupy the octahedral sites in equal proportions, and with  $\text{Fe}^{3+}$  being the sole component of the tetrahedral sites. With increasing temperature, cation distribution disorders towards the

Communicated by Othmar Müntener.

**Electronic supplementary material** The online version of this article (<https://doi.org/10.1007/s00410-020-01679-z>) contains supplementary material, which is available to authorized users.

✉ R. H. Sievwright  
robsievw@gmail.com

<sup>1</sup> Department of Earth Science and Engineering, Imperial College London, London SW7 2AZ, UK

<sup>2</sup> Department of Earth Sciences, LODE, Natural History Museum, Cromwell Road, London SW7 5BD, UK

<sup>3</sup> Research School of Earth Sciences, Australian National University, Canberra, ACT 2601, Australia

random arrangement of maximum configurational entropy,  $[A_{1/3}B_{2/3}][A_{2/3}B_{4/3}]O_4$  (Wu and Mason 1981). Magnetite is stable between the iron–magnetite or wüstite–magnetite oxygen buffers (depending on temperature) at low  $fO_2$  and the hematite–magnetite oxygen buffers at high  $fO_2$  where its stoichiometry deviates somewhat from the ideal of three cations to four oxygens, depending also on temperature (e.g. O'Neill 1988). These deviations from the ideal stoichiometry have been shown to have a profound effect on diffusion. Under oxidizing conditions, magnetite is cation deficient ( $Fe/O < 3/4$  atomic), with vacancies on the normally occupied octahedral and/or tetrahedral cation sites. However, at low  $fO_2$ , where magnetite is at, or near, equilibrium with wüstite, magnetite has a slight excess of cations accommodated at interstitial sites. As a result, it has been proposed that an interstitialcy diffusion mechanism predominates at low  $fO_2$ , whereas a vacancy diffusion mechanism prevails under more oxidising conditions (Van Orman and Crispin 2010). Hence understanding diffusion in magnetite mandates that  $fO_2$  should be studied as a variable.

The diffusion of some cations (Fe, Co, Cr, Al and Ni) in magnetite have been studied over a range of physical conditions (Dieckmann et al. 1978; Dieckmann and Schmalzried 1986; Aggarwal and Dieckmann 2002). However, diffusion properties for the less compatible trace elements are not well known. Consequently, the diffusion coefficients for > 21 elements were investigated in natural magnetite as a function of  $fO_2$  ( $FMQ-1 \leq fO_2 \leq FMQ+4.89$ ) at 1150 °C and 1 bar by equilibration with a synthetic silicate melt reservoir. This experimental approach also allows equilibrium partition coefficients to be derived from element concentrations at the magnetite–glass interface.

## Experimental procedures

The experimental approach applied here follows that of Spandler and O'Neill (2010). Silicate melt is held inside a crucible made from a single crystal of magnetite, to form a diffusion couple between melt and magnetite. The magnetite crystals used (known as Mt-1) have a restricted compositional range, which is close to pure magnetite, with total trace element contents less than 1500 ppm. The composition of the silicate melt is designed to have a major-element composition in equilibrium with the magnetite under the experimental run conditions, to ensure that negligible crystallisation or dissolution of magnetite occurs at the magnetite–melt interface. The melts were doped with trace elements, and the experiments were run for sufficient time to generate diffusion profiles in the magnetite that can be measured using scanning

laser-ablation inductively-coupled-plasma mass-spectrometry (LA-ICP-MS).

## Synthesis of trace-element doped melt

Since the composition of the melt in equilibrium with magnetite changes with  $fO_2$ , different synthetic CaO–FeO–SiO<sub>2</sub> (CFS) melts were prepared for each run condition. Other major elements such as Al, Mg and Ti were not added to the synthetic melt as major components because their partitioning could have altered the major element chemistry of the magnetite and, therefore, its structure and diffusion properties.

A primary CFS mix was prepared with FeO = 25 wt. %, CaO = 15 wt. % and SiO<sub>2</sub> = 60 wt. % from a mixture of synthetic oxides (SiO<sub>2</sub> and Fe<sub>2</sub>O<sub>3</sub>) and carbonates (CaCO<sub>3</sub>). To obtain the composition of the melt needed for each  $fO_2$  condition, preliminary experiments were conducted as follows. An aliquot of this primary CFS mix was combined with finely ground magnetite to form a paste, which was pressed onto 0.3 mm diameter Pt wire loops. The Pt wire loops were then suspended in the hot zone of a GERO 1-atm vertical furnace at 1150 °C with gas mixing ratios set to produce the specified  $fO_2$  conditions. Samples were held in the furnace for 12 h before drop-quenching into distilled water. The experimental charges consisted of magnetite, quartz and glass (quenched melt). The composition of the glass in equilibrium with the magnetite and quartz was analysed via scanning electron microscopy electron-dispersive-spectroscopy (SEM–EDS) using a JEOL 6400 SEM; analytical conditions were 20 kV accelerating voltage, 3 nA sample current and 1 µm spot size. The derived compositions represent the experimental CFS starting compositions to be used for each respective  $fO_2$ . Separate starting compositions for each  $fO_2$  condition were then prepared using dried oxides and carbonates and decarbonated as done for the primary starting material. The bulk chemical compositions of the starting materials used are provided in Table 1.

Trace elements were added to each separate starting composition as inductively coupled plasma (ICP) standard solutions using a pipette in proportions necessary to dope the starting material at approximately 200 ppm for all trace elements. Aluminium, Co, Cr, Cu, Hf, In, Mg, Mn, Mo, Nb, Ni, Th, Ti, Sc, Sr, Ta, U, V, W, Y, Zn, Zr, Lu, Y were added in all experiments, Li in experiments at FMQ–1, FMQ and FMQ + 4.89 and Ga in experiments at FMQ–1. Each mixture was dried under a heat lamp, homogenized in an agate mortar, and denitrified at 500 °C for 2 h.

## Preparing magnetite crucibles

Euhedral natural magnetite crystals measuring more than 6 mm length and 6 mm in diameter were selected. SEM

**Table 1** Major element composition of experimental starting materials

Experiment	n	SiO <sub>2</sub> (wt. %)	CaO (wt. %)	FeO (wt. %)
MB– 24 (FMQ–1)	12	31.0 (3)	7.1 (2)	62.0 (4)
MB– 21 (FMQ)	14	37.0 (4)	8.5 (3)	54.5 (5)
MB– 7 (FMQ+1)	13	44.5 (2)	12.60 (4)	42.9 (2)
MB– 2/3/9 (FMQ+2)	23	47.6 (2)	18.60 (7)	33.5 (2)
MB– 14 (FMQ+3)	14	49.6 (2)	21.48 (7)	28.9 (2)
MB– 23 (FMQ+4.89)	14	49.2 (3)	22.9 (3)	27.9 (3)

Uncertainty in last significant figure (in brackets) = 1  $\sigma$  of multiple (*n*) analyses

These compositions were determined by running preliminary experiments to assess the composition of silicate melt in equilibrium with magnetite (Mt–1)

back-scattered electron (BSE) images confirmed that the magnetite crystals were inclusion free and their compositions were checked via LA–ICP–MS. The crystals were mounted in epoxy resin and then carefully drilled with a diamond drill bit to produce a cylindrical cavity 1.25–2.5 mm in diameter and 3–4 mm long. The epoxy was then carefully removed with pliers after softening in an oven at 120 °C and the crucibles were finally cleaned with ethanol and distilled water in an ultrasonic bath.

Each magnetite bucket was filled with the appropriate powdered starting material and hung by Pt wire in a GERO 1-atm vertical gas-mixing furnace, with  $fO_2$  conditions set to those required using a flowing CO<sub>2</sub>/CO mixture. The magnetite was loaded into the furnace at 600 °C, then the temperature was ramped at 200 °C/h to 1150 °C and left to anneal for the required duration of the experiment. A relatively slow ramping rate was necessary to minimize cracking of the buckets and prevent the melt escaping from the bucket. Finally, the run product was drop quenched into distilled water, dried, mounted into epoxy and polished perpendicular to the cylindrical cavity for analysis.

### Experimental conditions

All experiments were conducted at 1 bar, 1150 °C with  $fO_2$  varied from FMQ–1 to FMQ+4.89. 12 h was sufficient time to generate diffusion profiles greater than 30 microns for most elements studied, which are sufficiently long to interpret reliable interface concentrations, initial concentrations and diffusion constants for the different elements. However, two experiments were run at longer durations (66.9 and 161.4 h) to check for consistency with the 12-h experiments (Table 2).

**Table 2** Experimental conditions

Experiment	<i>T</i> (°C)	$fO_2$ ( $\Delta$ FMQ <sup>a</sup> )	<i>t</i> (h) <sup>b</sup>
MB– 3	1150	FMQ+2.0	11.99
MB– 2	1150	FMQ+2.0	161.44
MB– 9	1150	FMQ+2.0	66.93
MB– 7	1150	FMQ+1.0	12.38
MB– 14	1150	FMQ+3.0	12.12
MB– 21	1150	FMQ+0.0	11.99
MB– 23	1150	FMQ+4.9	12.00
MB– 24	1150	FMQ–1.0	12.28

<sup>a</sup> $\Delta$ FMQ = log  $fO_2$  (experiment) – log  $fO_2$  (FMQ buffer); values were calculated using O'Neill (1987)

<sup>b</sup>Time represents dwell time in hours after ramp up to final temperature

### Analytical methods

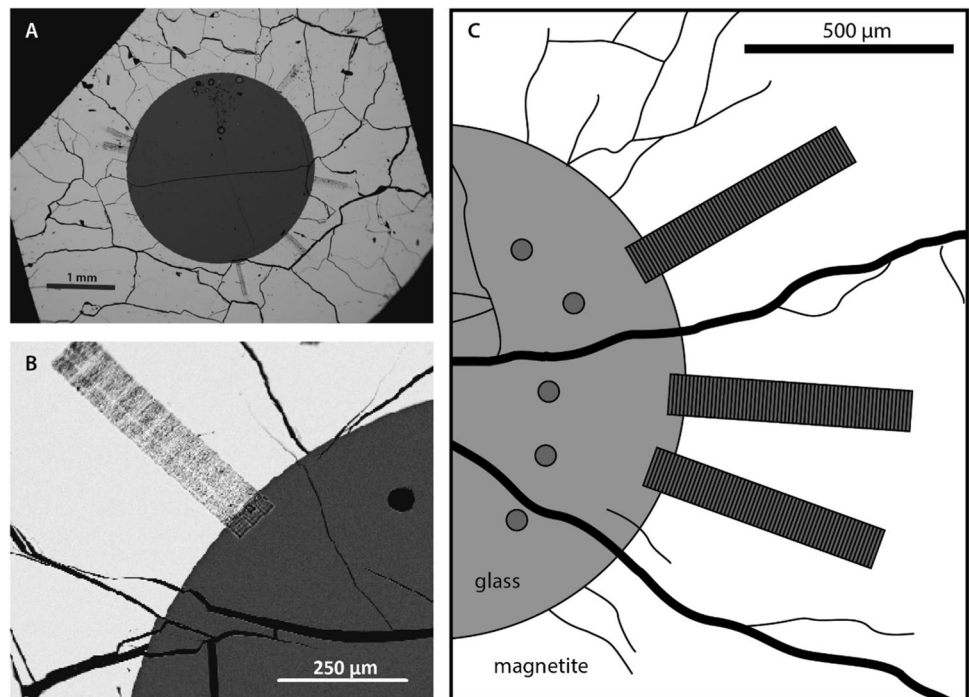
Run products were first examined using a JEOL 6400 SEM at the Research School of Earth Sciences (RSES), Australian National University (Fig. 1). Back-scattered electron imaging was used to inspect the magnetite interface, to identify whether there had been discernible crystallisation or dissolution, which could distort diffusion profiles.

A Cameca SX-100 electron microprobe (EPMA) at the Natural History Museum, London, was used to measure major element contents of the silicate glass. Calcium, Si and Fe were analysed. A 20 kV accelerating voltage, 2 nA sample current and a defocused (10–20  $\mu$ m) beam were applied.

Trace-element compositions of magnetite and glass were analysed using LA–ICP–MS at the RSES and at the LODE Research Facility at the Natural History Museum, London. The LA–ICP–MS at the RSES consists of an Agilent 7700  $\times$  quadrupole ICP–MS coupled to a Resonetics 193 nm excimer laser with a custom-built ablation chamber. At the LODE Research Facility, a New Wave Research 193 nm excimer laser coupled to an Agilent 7700  $\times$  quadrupole ICP–MS was used. Laser energy was regulated to provide a laser fluence at the sample site of 3.5 J/cm<sup>2</sup> (ANU) and 3.2 J/cm<sup>2</sup> (LODE). The ICP–MS was tuned prior to analyses to ensure low backgrounds and low oxide production levels.

Rectangular ablation shapes were used to improve the resolution of an element concentration profile in comparison to profiles obtained using conventional circular ablation shapes. For each traverse, the laser was focused into a 100  $\times$  6 micron rectangular beam oriented parallel to the magnetite–glass interface, as observed with an optical microscope. After background counting for 30 s, the laser was switched on and the sample traversed continuously beneath the laser at a rate of 1 micron/s. All traverses were started in the interior of the magnetite crystal and ended

**Fig. 1** Geometry of experimental products and analytical procedure. **a, b** SEM–BSE images of magnetite crystal containing quenched glass post-analysis with LA–ICP–MS showing laser traverse profiles. **c** Cartoon of the magnetite–glass interface region showing laser-ablation profiles through magnetite and glass and laser ablation pits in glass



by ablating clean glass; this avoided analyses of previously ablated glass that could have been deposited at the magnetite–glass interface. The traverses were positioned as far from cracks as possible. Glass was separately analysed with a 50 micron laser spot size. Fe and Ca were used as an internal standard for the magnetite and glass analyses, respectively, measured previously via EPMA. BCR-2g was used as an external standard for magnetite analyses (other than In, for which GSD-1g was used) and NIST 610 for glass analyses. GSD-1g and GSE-1g were also measured for quality control monitoring. All reference materials were analysed in the same fashion as the sample analysed. The isotopes analysed were  $^7\text{Li}$ ,  $^{24}\text{Mg}$ ,  $^{27}\text{Al}$ ,  $^{29}\text{Si}$ ,  $^{43}\text{Ca}$ ,  $^{45}\text{Sc}$ ,  $^{49}\text{Ti}$ ,  $^{51}\text{V}$ ,  $^{52}\text{Cr}$ ,  $^{55}\text{Mn}$ ,  $^{57}\text{Fe}$ ,  $^{59}\text{Co}$ ,  $^{60}\text{Ni}$ ,  $^{63}\text{Cu}$ ,  $^{65}\text{Cu}$ ,  $^{66}\text{Zn}$ ,  $^{69}\text{Ga}$ ,  $^{88}\text{Sr}$ ,  $^{89}\text{Y}$ ,  $^{90}\text{Zr}$ ,  $^{92}\text{Zr}$ ,  $^{93}\text{Nb}$ ,  $^{95}\text{Mo}$ ,  $^{115}\text{In}$ ,  $^{175}\text{Lu}$ ,  $^{177}\text{Hf}$ ,  $^{181}\text{Ta}$ ,  $^{182}\text{W}$ ,  $^{232}\text{Th}$  and  $^{238}\text{U}$ . For the majority of analyses, Lu, Y and Th were measured using a 0.3 s dwell time on each isotope; the other isotopes were measured with 0.1 s dwell times. Some slow diffusing elements (Sc, Ti, V, Zr, Nb, Hf, Ta) were also measured separately, thereby reducing the ICP–MS sweep time to 0.7 s which increased analytical precision. For most traverses, the sweep time for the ICP–MS was 2.0 s. Data were reduced using IOLITE software in a ‘natural’ fashion, such that each ablation slice was processed individually.

#### Calculation of diffusion and partition coefficients

The diffusion geometry is assumed to be that of one-dimensional diffusion into a semi-infinite medium with a constant concentration boundary condition maintained at the

magnetite–melt interface. These conditions require element diffusion in the melt to be fast with respect to element diffusion in magnetite, which is deemed reasonable on account of very fast element diffusivities in silicate melts at high temperatures (Spandler and O’Neill 2010). Furthermore, the melt compositions used here are relatively low silica (<50 wt. %  $\text{SiO}_2$ ) and diffusivities generally increase with decreasing  $\text{SiO}_2$  (Henderson et al. 1986). The solution to the diffusion equation under these conditions is (Crank 1975):

$$\frac{c_i - c(x)}{c_i - c_0} = \text{erf}\left(\frac{x}{2(D_M t)^{1/2}}\right) \quad (1)$$

Here,  $D_M$  is the chemical diffusion coefficient,  $c(x)$  the concentration at distance  $x$  into the magnetite,  $c_i$  the concentration at the interface ( $x=0$ ),  $c_0$  the initial concentration in magnetite and  $t$  is the duration of the experiment, taken from when the heating ramp reached the equilibration temperature of 1150 °C. This equation applies to element diffusion both into and out of the magnetite.

The relatively slow ramping rate of 200 °C/h raises the possibility of some experimental error in the time of the diffusion anneals. An effective time ( $t_{\text{eff}}$ ), equivalent to the time that would be required at the equilibration temperature (1423 K) to achieve the same amount of diffusion, may be calculated from:



$$t_{\text{eff}} = \left( \int_0^{t_f} D(t) dt \right) / D_{1423 \text{ K}} \quad (2)$$

Assuming that the diffusion coefficients vary with temperature according to the Arrhenius relationship, with constant activation energies  $H$ , their variation with time during the ramp would be:

$$D(t) = D_0 \exp \left\{ -H / \left( R \left( T_o + \left( \frac{dT}{dt} \right) t \right) \right) \right\} \quad (3)$$

where  $\frac{dT}{dt}$  is the ramp rate. Substituting this relation into Eq. 2 gives:

$$t_{\text{eff}} = \left( \int_0^{t_f} \left( \exp \left\{ -H / \left( R \left( T_o + \left( \frac{dT}{dt} \right) t \right) \right\} dt \right) / \exp \left\{ \frac{-H}{1423R} \right\} \right) \right) \quad (4)$$

Cation diffusion in oxides generally has activation energies between 200 and 300 kJ/mol (Van Orman and Crispin 2010), corresponding in these experiments to values of 0.37 and 0.25 h, respectively, from numerical integration of Eq. 4. These values are 3% and 2% of the shortest equilibration time used in this study, 12 h, well below other experimental uncertainties. In addition, the times calculated from Eq. 4 may be overestimated as diffusion presumably only gets going when the contents of the buckets melt and wet the walls. In magnetite, however, the situation is complicated by the dependence of cation diffusivity on  $f\text{O}_2$ , values of which also depend on temperature and, therefore, also vary continuously during the ramp. Furthermore, the magnetite crystals in principle need some time to equilibrate their point-defect concentrations with the imposed  $f\text{O}_2$ . In view of these complexities, it is more appropriate to evaluate whether the ramp time has any effect by comparing results from the three experiments run for 12.0, 66.9 and 161.4 h under otherwise identical conditions (Table 2).

Diffusion profiles across the inner edges of the magnetite crucibles into the glass were evaluated by plotting element concentrations versus distance. The position of the interface in each profile was determined from the abrupt change in concentrations of most elements in the profiles (Fig. 2). It is worth noting that given the width of the rectangular laser beam (6  $\mu\text{m}$ ), the interface position may be inaccurate by up to 3  $\mu\text{m}$ . The abrupt change in concentrations of most elements at the interface did vary for some analytical traverses by up to 5 microns, corresponding to 5 s of continuous analysis. The increase becomes noticeable earlier for very incompatible elements, due to imperfect alignment of the slit with the interface. In such cases, the last few microns of the profile were excluded,

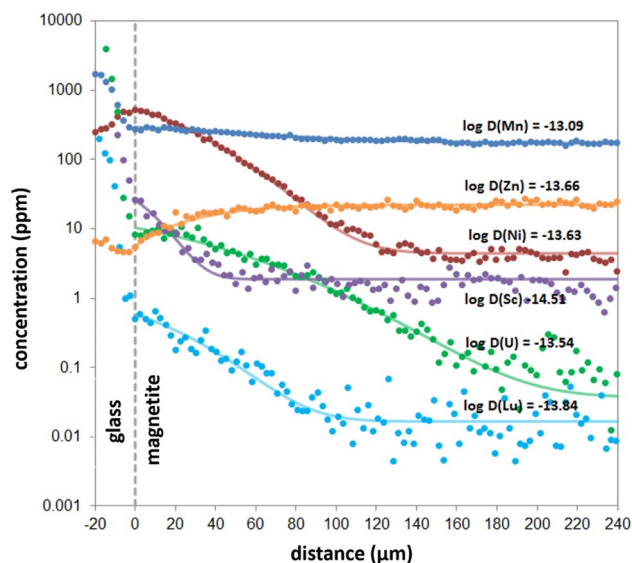


**Fig. 2** Representative diffusion profiles for Mn, Zn, Ni, Sc, U and Lu acquired by LA-ICP-MS analysis for experiment MB-7 at  $f\text{O}_2 = \text{FMQ} + 1$ ,  $t = 12$  h. Solid curves represent the best fits to the data according to the diffusion equation. Dashed vertical line at 0  $\mu\text{m}$  is the magnetite–glass interface

and this part was extrapolated to the glass interface using the remainder of the diffusion profile within the magnetite. The uncertainties caused by the uncertainty in the interface position with the scanning method have been discussed by Zhukova et al. (2014). They are more significant for partition coefficients than diffusion coefficients.

The data were fitted directly to the diffusion equation using the known values,  $c(x)$ ,  $x$  and  $t$ , and solving for  $c_i$ ,  $c_o$  and  $D_M$  using weighted, multiple, non-linear least squares. The accuracy of each fit was checked graphically by comparing the calculated and measured diffusion profiles. With the exception of volatile elements (e.g. In, Zn), whose diffusion profiles are modified by decreasing concentrations with time in the melt, only those diffusion profiles which were described well by the diffusion equation were accepted. Poor fits could occur if the profile was not close enough to perpendicular to the interface, or if the profile was distorted by element diffusion from melt in a crack. Examples of the fits are given in Fig. 2.

The parameters  $c_i$ ,  $c_o$  and  $D_M$ , were obtained for each element in each diffusion profile. Consistent values of  $D_M$ ,  $c_i$  and  $c_o$  across all experiments provide a check on data quality and the standard deviation of these multiple values was used to estimate the experimental uncertainties. As an additional means of verification of the values of  $c_o$ , analyses using LA-ICP-MS with a 100 micron spot were conducted at the outside of the magnetite bucket and distal from the melt, in regions not influenced by element diffusion from the melt for most elements. Even with a 100 micron laser spot,

a number of elements were not above the limit of detection. For these elements,  $c_o$  was approximated as 0 ppm when solving for  $c_i$  and  $D_M$ .

Values of the magnetite/melt partition coefficients ( $K_M$ ) can be calculated from  $K_M = c_i/c_{liq}$ , where  $c_{liq}$  is the concentration in the liquid, and  $c_i$  is the interface concentration. The uncertainty in  $K_M$  for each element in each experiment was propagated from the standard deviations of multiple  $c_i$  and  $c_{liq}$  determinations. For some analytical traverses, it was not possible to extract a viable diffusion profile whilst still being possible to interpret  $c_i$ . For example, in some analytical traverses pre-existing inclusions in the magnetite interrupted the diffusion profile. However, it was still usually possible to obtain  $c_i$ , and thus calculate  $K_M$ .

## Results

### Magnetite (Mt–1) composition

Multiple analyses of four separate magnetite (Mt–1) crystals prior to experiments indicated a uniform major and trace element composition (Table 3). However, some minor

**Table 3** Composition of magnetite crystals (Mt–1) prior to annealing which was used in experiments

Element	Mean Concentration (ppm)*	Element	Mean Concentration (ppm)*
Li	0.91 (3)	Zn	26 (3)
Mg	260 (71)	Ga	2.3 (5)
Al	230 (57)	Y	<dl
Si	230 (38)	Zr	<dl
Ca	<dl	Nb	<dl
Sc	0.9 (3)	In	<dl
Ti	230 (56)	Mo	0.02 (1)
V	40 (17)	Lu	<dl
Cr	10 (7)	Hf	<dl
Mn	100 (20)	Ta	<dl
Co	2.0 (3)	W	<dl
Ni	3.9 (7)	Th	<dl
Cu	<dl	U	<dl

\*Errors (in last 1 or two significant figures, in brackets) =  $1\sigma$  of 40 analyses (10 on each of four separate magnetite crystals)

**Table 4** Starting composition and final glass compositions for experiments at  $fO_2 = FMQ + 2$  and  $T = 1150$  °C

	Starting mix	Glass @ 12.0 h	Glass @ 66.9 h	Glass @ 161.4 h
SiO <sub>2</sub> (wt. %)	47.6	47.1 (2)	46.3 (1)	48.4 (2)
CaO (wt. %)	18.6	18.0 (1)	20.8 (1)	23.7 (2)
FeO (wt. %)	33.5	34.9 (2)	32.9 (1)	27.8 (3)

SiO<sub>2</sub>, CaO and FeO were measured using EPMA. Data are normalized to 100% anhydrous errors =  $1\sigma$

exsolution for elements such as Mg and Ti meant it was sometimes difficult to measure clean diffusion profiles for these elements. Prior to the experiment, most trace element contents are very low in the natural magnetite. Only Mg, Al, Si, P, Sc, Ti, V, Cr, Mn, Co, Ni, Zn, Ga and Mo were above the limit of detection with LA–ICP–MS using a 100 micron spot and GSD-1g as the external standard. The total trace element content of all elements detectable with LA–ICP–MS is less than 1500 ppm.

Post-experimental, annealed magnetite crystals have trace element contents in the outer edge of the crucibles (in regions unaffected by element diffusion) in agreement with the initial composition of Mt–1, apart from Cu and Li. Furthermore, in all experiments,  $c_o$  values refined from least-squares regressions are similar to the concentrations measured in the original magnetite for elements which are above the limit of detection. Values of  $c_i$ ,  $c_o$  and  $\log D$  determined using LA–ICP–MS data generated at RSES and LODE were consistent for all elements analysed. Some particularly incompatible elements (e.g. Sr and Th) were not doped at sufficient concentrations to raise  $c_i$  above the limit of detection in most experiments.

### Glass composition

The starting glass and final glass post– experiment are very similar in composition. For the 12 h experiments, the final glass differs from the initial composition by < 1.5 wt % for Ca, Fe and Si. This is important because it indicates that the composition of the melt remained relatively constant for the duration of the experiments. Some experiments have rare crystals of magnetite and quartz (e.g. Fig. 1a) nucleated within sections of the melt, the abundance of which increases with experiment duration. This resulted in a progressive decrease in FeO and SiO<sub>2</sub> concentrations, and concomitant increase in CaO concentrations in comparison to the starting composition, with increasing experiment duration (Table 4).

With increasing  $fO_2$ , there is a significant change in the major element chemistry of the melt in equilibrium with the magnetite (Table 1). Between  $FMQ - 1 < fO_2 < FMQ + 4.89$ , the FeO content decreases from 62.0 to 27.9 wt. %, the CaO content increases from 7.1 to 22.9 wt. %, and the SiO<sub>2</sub> content increases from 31.0 to 49.2 wt. % (Table 1).

## Bulk loss of trace elements

Several elements could be susceptible to bulk loss during experiments due to their volatility. For example, although added at an initial concentrations  $> 200$  ppm, the concentrations of Zn and In in the final glass were  $< 1.4$  ppm and  $< 8.8$  ppm, respectively, at  $fO_2 = FMQ - 1$ , and exhibited increasing loss with decreasing  $fO_2$  and with increasing duration of the experiment. In the case of In, it was clear that In was volatile at low  $fO_2$  from the deviation in the fit of the diffusion profiles from Eq. 1. This effect was only apparent in experiments with low  $fO_2$  ( $fO_2 \leq FMQ + 1$ ).

Copper concentrations in the glass were significantly lower than expected and decreased with experimental duration in experiments conducted at the same  $fO_2$  and  $T$  conditions ( $FMQ + 2 / 1150$  °C). This could be due to volatility, but it is also possible that the particularly fast diffusion for Cu meant a large amount of Cu was removed from the melt to the magnetite crucible. Chromium, V and Ni contents in the glass were also significantly less than 200 ppm, plausibly due to high magnetite-melt partition coefficients. These latter depletions have a relatively minor effect on calculated diffusion coefficients.

## Partition coefficients

The results for  $c_i$ ,  $c_{melt}$  and  $K_M$  are listed in Supplementary Table S1. At least three values were measured for each element in each experiment, and the mean value of these was used to calculate  $K$ . In the realm of Henry's Law, partition coefficients will be independent of the concentration of the trace element. It has been suggested that Henry's Law will be satisfied as long as the concentrations in the crystal are less than 1 wt. % (Prowatke and Klemme 2006), which is the case for the interface concentration of all trace elements in the magnetite crystals studied here.

The derived partition coefficients for a subset of 16 of the elements studied are in excellent agreement with literature data acquired under similar conditions ( $FMQ + 2$  and  $1220$  °C—Fig. 3; Wijbrans et al. 2015). Nevertheless, differences should be expected considering the different magnetite composition and temperature.

## Monovalent cations

Lithium partitioning into magnetite increases with increasing  $fO_2$ , particularly at  $fO_2 > FMQ$  (Fig. 4a). Lithium was not added to the  $FMQ + 1$ ,  $FMQ + 2$  or  $FMQ + 3$  starting materials, however, a trace amount was still present in these melts enabling  $K$  to be determined for  $FMQ + 3$ . In this experiment, Li diffused out instead of into magnetite.

Copper exhibits similar partitioning behaviour to Li, with a strong correlation between  $K(Cu)$  and  $K(Li)$ . As mentioned

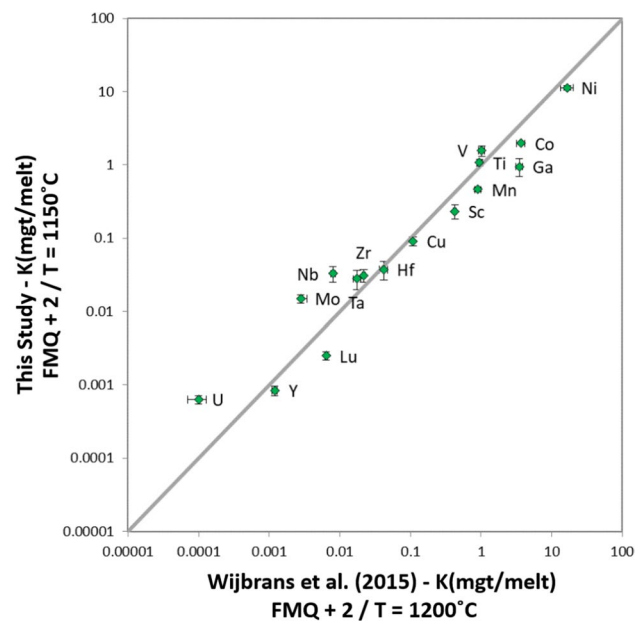


**Fig. 3** Partition coefficient data acquired in this study compared with results from Wijbrans et al. (2015). Note, Wijbrans et al. (2015) studied spinel with a 54% magnetite component, compared to the 100% magnetite used in this study. Grey line is 1:1. Error bars =  $1\sigma$  of multiple analyses

previously, there was significant Cu loss during experimental runs, particularly at high  $fO_2$  and over experimental durations more than 12 h. However, despite the low concentrations of Cu, there is a clear linear trend for  $K(Cu)$  with  $fO_2$  for experiments conducted at  $t = 12 \pm 0.4$  h (Supplementary Fig. S1).

## Divalent cations

The magnetite-melt partition coefficients of Mg, Mn, Co and Ni all correlate with one another suggesting a similar control on their behaviour. Nickel is most compatible, followed by Co, Mn and Mg. These cations exhibit an increase in  $K$  with increasing  $fO_2$ ; between  $FMQ - 1 \leq fO_2 \leq FMQ + 4.89$ ,  $K(Mn)$  increases from 0.24 to 1.08,  $K(Co)$  increases from 0.94 to 4.50 (Fig. 4b),  $K(Ni)$  increases from 3.01 to 18.41 and  $K(Mg)$  increases from 0.20 to 0.66.

It was generally difficult to measure accurate interface concentrations for Ca as a result of the large contrast between the Ca content of the melt (a major element in the melt composition) and the low concentration at the magnetite–glass interface. Consequently,  $K(Ca)$  values are not supported by as large a number of  $c_i$  values as for other divalent cations and should, therefore, be viewed with caution. Nonetheless, where it was possible to calculate  $K(Ca)$ , there is a good correlation between  $K(Ca)$  and the other divalent cations. As mentioned previously Zn was lost during

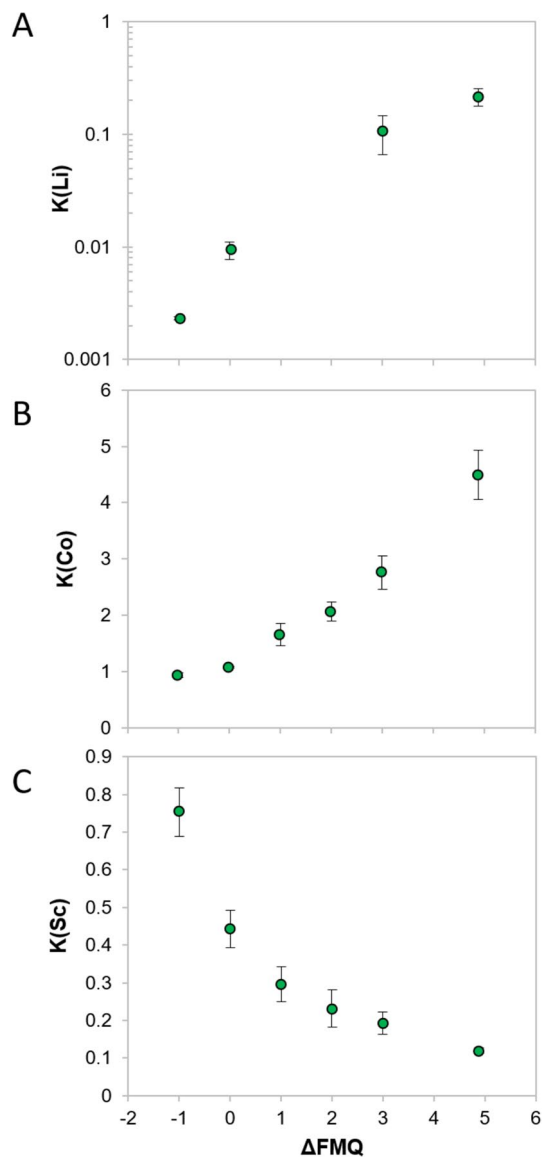


**Fig. 4** Magnetite-melt partition coefficients ( $K$ ) for **a** Li, **b** Co and **c** Sc as a function of  $f\text{O}_2$ .  $\Delta\text{FMQ} = \log f\text{O}_2$  (experiment)  $-\log f\text{O}_2$  (FMQ buffer); values were calculated using O'Neill (1987). Error bars =  $1\sigma$

the experiments. Given that the initial concentration of Zn in Mt-1 was relatively high, this resulted in bulk diffusion out of the crystal (Fig. 2). The decrease in  $c_i$  values for Zn leads to anomalous values for  $K(\text{Zn})$ , particularly at low  $f\text{O}_2$  values. Consequently, values for  $K(\text{Zn})$  are not considered reliable.

### Trivalent cations

$K$  values for the trivalent cations, Al, Sc, Ga, Y and Lu correlate positively, suggesting a similar control on their magnetite-melt partitioning behaviour. Gallium is the most

compatible, followed by Al, Sc, Lu and Y. With increasing  $f\text{O}_2$ , there is a decrease in the partition coefficient for all trivalent cations. Between  $\text{FMQ}-1 \leq f\text{O}_2 \leq \text{FMQ}+4.89$ ,  $K(\text{Al})$  decreases from 1.05 to 0.11,  $K(\text{Sc})$  decreases from 0.75 to 0.12 (Fig. 4c),  $K(\text{Ga})$  decreases from 2.79 to 0.32,  $K(\text{Cr})$  decreases from 197 to 0.11, and  $K(\text{Y})$  decreases from 0.0026 to 0.00051.

Cr is significantly more compatible in magnetite than any other element studied, with a partition coefficient as high as 197. Despite this, there are large errors associated with the  $K(\text{Cr})$  values as a result of particularly slow diffusion which meant the exact concentration of Cr at the magnetite–glass interface was difficult to determine precisely.  $K(\text{Cr})$  correlates positively with  $K$  values for other trivalent cations suggesting that Cr is incorporated predominantly as a trivalent cation. However, Cr is known to exhibit variable valence state as a function of  $f\text{O}_2$  and the  $\text{Cr}^{2+}/\Sigma\text{Cr}$  ratio has been shown to vary from 0.45 at  $\text{FMQ}+0.61$  (Ni–NiO  $f\text{O}_2$  buffer) to 0.9 at  $\text{FMQ}-3.1$  (iron-wüstite  $f\text{O}_2$  buffer) in a basaltic melt at 1400 °C (Schreiber and Haskin 1976; Roeder and Reynolds 1991; Berry and O'Neill 2004). A minor amount of  $\text{Cr}^{6+}$  can also occur at particularly high  $f\text{O}_2$  ( $\text{FMQ}+4.38$ ; Berry et al. 2006).

Loss of indium (presumed to be due to volatility) was evident, particularly at low  $f\text{O}_2$ , which produced hump-shaped diffusion profiles because of a decrease in the concentration of In in the melt during some experiments. Thus,  $K(\text{In})$  values measured at  $f\text{O}_2 = \text{FMQ}-1$  (MB-24);  $\text{FMQ}$  (MB-21) and  $\text{FMQ}+4.89$  (MB-23) are not considered to be as accurate as for other elements.

### Tetravalent, pentavalent and hexavalent cations

Titanium and the HFSEs (Zr, Hf, Nb, and Ta) show similar partitioning behaviour and are decreasingly partitioned with increasing  $f\text{O}_2$ . Titanium ranges from being compatible at  $f\text{O}_2 < \text{FMQ}+3$  to incompatible at higher  $f\text{O}_2$ , whereas the HFSEs are incompatible over the entire range of  $f\text{O}_2$  studied. Between  $\text{FMQ}-1 \leq f\text{O}_2 \leq \text{FMQ}+4.89$ ,  $K(\text{Ti})$  decreases from 4.97 to 0.22,  $K(\text{Nb})$  decreases from 0.52 to 0.0024,  $K(\text{Hf})$  decreases from 0.50 to 0.007,  $K(\text{Ta})$  decreases from 0.33 to 0.0024 and  $K(\text{Zr})$  decreases from 0.30 to 0.006. There is also an excellent correlation between the partitioning of trivalent cations, Ti and HFSEs, although the range of partition coefficients does not vary as much for the trivalent cations as for Ti and the HFSEs. In comparison to the HFSEs, there is a paucity of data for Ti due to minor pre-existing exsolution in the magnetite disturbing the Ti diffusion profiles. The HFSEs and other tetravalent, pentavalent and hexavalent cations, however, were much less frequently interrupted by exsolution. Furthermore, the minor increase in Ti content in exsolved sections did not affect the diffusion of other elements, as evinced by a good fit to the diffusion



equation through exsolved regions. Silicon concentrations in the annealed magnetites were much elevated over those in the crystals analysed before annealing, but the diffusion profiles across the crystals were flat (Supplementary Fig. S2). This implies either that the analysed Si is an artefact of unknown origin, or that the four unannealed crystals chosen for analysis were somehow not representative in their Si contents of the crystals used in the diffusion experiments, or, if the elevated levels are real, that diffusion of Si in magnetite is extraordinarily fast. In support of the latter, we note that there is a weak correlation between  $K(\text{Ti})$  and  $K(\text{Si})$ . Nevertheless, we feel that this implied fast diffusion is so unexpected as to require future experimental replication for its affirmation.

Vanadium partitioning decreases with increasing  $f\text{O}_2$  (Fig. 5b) and, like Ti, changes from compatible at  $f\text{O}_2 < \text{FMQ} + 3$  to incompatible at higher  $f\text{O}_2$ . A complication of interpreting V partitioning, as discussed in Sievwright et al. (2017), is that V occurs as  $\text{V}^{3+}$ ,  $\text{V}^{4+}$  and  $\text{V}^{5+}$  in silicate melts across the range of  $f\text{O}_2$  studied, and as  $\text{V}^{3+}$  and  $\text{V}^{4+}$  in magnetite, independent of  $f\text{O}_2$ , due to the electron exchange reaction  $\text{V}^{3+} + \text{Fe}^{3+} = \text{Fe}^{2+} + \text{V}^{4+}$  (O'Neill and Navrotsky 1984).  $K(\text{V})$  values reported here follow a similar trend with  $f\text{O}_2$  to those reported by Toplis and Corgne (2002) for a Ti-bearing ferrobaltic system (Fig. 5b), but are slightly offset to lower values. It is likely that the lower  $K(\text{V})$  values are a result of the lower Ti contents of magnetite in this study (maximum Ti = 0.14 wt. %).

Uranium and W are highly incompatible in magnetite and their partition coefficients decrease with increasing  $f\text{O}_2$  (Fig. 5c), correlating with Ti, HFSEs and V. Tungsten, although a polyvalent cation, has been shown to occur principally as  $\text{W}^{6+}$  in the  $f\text{O}_2$  range studied (O'Neill et al. 2008), suggesting that W is incorporated into magnetite as a 6+ cation. Uranium can occur as  $\text{U}^{4+}$ ,  $\text{U}^{5+}$  or  $\text{U}^{6+}$  under conditions geologically relevant for Earth, although  $\text{U}^{4+}$  and  $\text{U}^{5+}$  are the most abundant species in silicate melts over the  $f\text{O}_2$  range studied (Halse 2014). The oxidation state of U in magnetite is unknown (see below). Thorium is strongly incompatible in magnetite with the lowest partition coefficient of any element investigated; the maximum  $K(\text{Th})$  value in this study is 0.00023. It was only possible to measure discernible diffusion profiles in two experiments at  $f\text{O}_2 < \text{FMQ} + 1$ . Nonetheless, the observed increase in  $K(\text{Th})$  with decreasing  $f\text{O}_2$  is comparable to the other tetravalent cations.

Molybdenum partitioning decreases with increasing  $f\text{O}_2$  but, unlike other tetravalent, pentavalent and hexavalent cations previously reported, exhibits a more substantial decrease in magnetite-melt partitioning between  $\text{FMQ} - 1$  and  $\text{FMQ}$ . Molybdenum in silicate melts occurs predominantly as a 6+ cation under the relatively oxidizing conditions of our experiments, only changing to predominantly 4+ at lower  $f\text{O}_2$  (Holzheid et al. 1994; O'Neill and Eggins 2002).

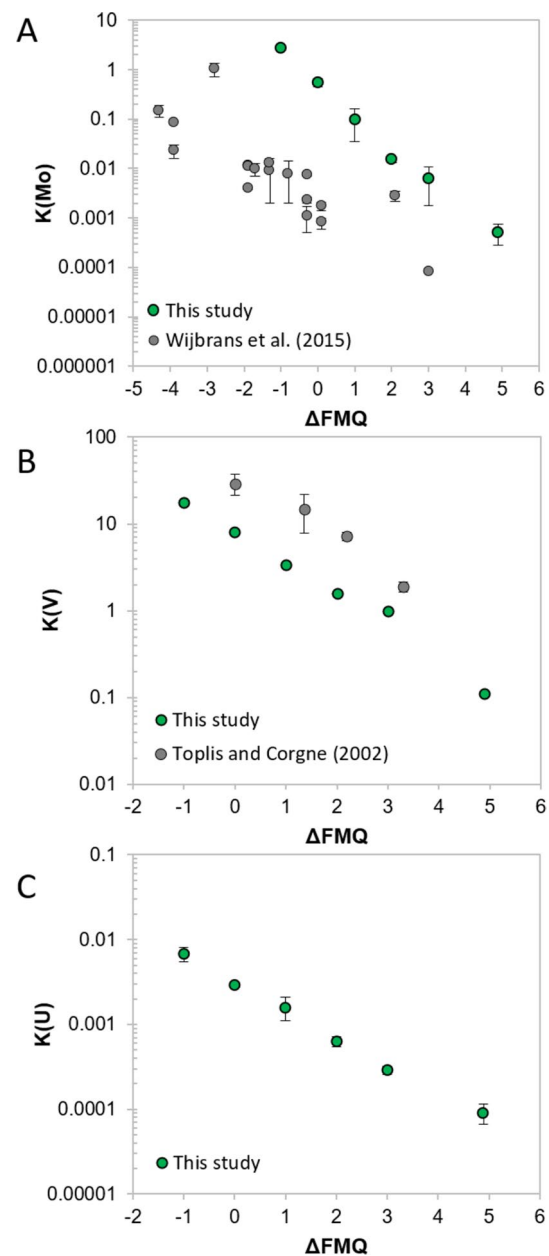


**Fig. 5** Magnetite-melt partition coefficients ( $K$ ) for **a** Mo, **b** V and **c** U as a function of  $f\text{O}_2$  for this study compared with previous work.  $\Delta\text{FMQ} = \log f\text{O}_2$  (experiment)  $- \log f\text{O}_2$  (FMQ buffer); values were calculated using O'Neill (1987). Error bars =  $1\sigma$

Molybdenum occurs in the spinel phases  $\text{Fe}_2\text{MoO}_4$  as 4+, and likely also in  $\text{Fe}_3\text{O}_4$ – $\text{Fe}_2\text{MoO}_4$  solid solutions (Katsura et al. 1975; O'Neill and Navrotsky 1984). Values of  $K(\text{Mo})$  follow a similar trend with  $f\text{O}_2$  to that reported by Wijbrans et al. (2015), who studied spinel–melt partitioning in more Cr-rich spinel but are generally higher (Fig. 5a).

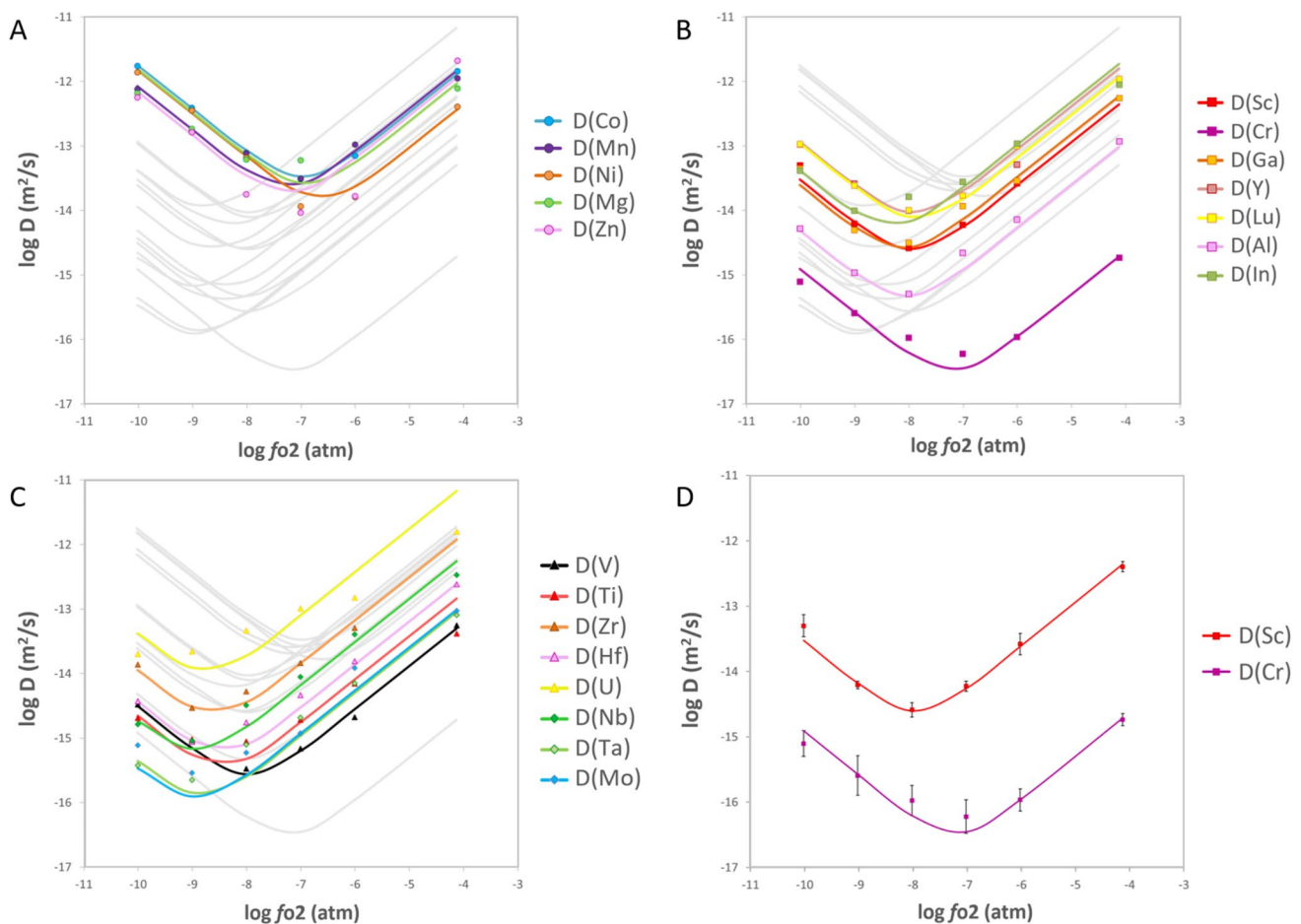


**Fig. 6** Variation in cation diffusion coefficients in magnetite as a function of  $fO_2$  for Co, Mn, Ni, Mg and Zn (a), Sc, Cr, Ga, Y, Lu, Al and In (b), and V, Ti, Zr, Hf, Nb, Ta, Mo and U (c). Fit of cation diffusion coefficients for all elements to Eq. 5 used to solve for a vacancy constant ( $D_v^1 = D_v \exp(-H_v/RT)$ ) and interstitial constant

( $D_i^1 = D_i \exp(-H_i/RT)$ ) with fixed exponents of  $fO_2$  to  $2/3$  and  $-2/3$  for the vacancy and interstitialcy terms, respectively. Error bars ( $1\sigma$ ) provided for Sc and Cr as an example in (D), but were not included in other figures for clarity

## Diffusion coefficients

Chemical diffusion coefficients ( $D$ ) are summarised in Supplementary Table S1 and presented as a function of  $fO_2$  in Fig. 6. For some traverses, it was sometimes not possible to quantify a diffusion coefficient because of features such as contamination of the diffusion profile from melt in a nearby crack. In these cases it was usually still possible to measure  $c_i$  so that there are generally more values for  $c_i$  than for  $D$ . Nonetheless, at least 2 or more  $D$  values were measured for each cation in each sample, and the  $D$  values reported represent the mean of these repeat analyses. Diffusion coefficients are generally in good agreement with each other, with uncertainties typically less than 0.2 log  $D$  units (one standard deviation—Fig. 6d).

Most elements doped in the melt diffused into magnetite, with a concentration at the interface significantly greater than the initial background concentration. Magnesium, Al,

Si and Ti are often present in minor exsolved or inclusion phases which meant it was not always possible to fit a diffusion profile. Furthermore, the concentrations of Al and Mg at  $c_i$  were often close to  $c_0$  so that the profiles were not as clearly defined as for other elements. Spot analyses of the magnetite in regions furthest from the silicate melt reservoir were checked against the original magnetite composition and used to verify  $c_0$ . For elements above the limit of detection in the initial magnetite crucible, apart from Li, most traverses reached  $c_0$  and were within the error of the concentration measured in the original magnetite. In some cases, however, where the concentration of a given element in an analytical traverse did not reach  $c_0$ , the concentration determined from the spot analysis was used as  $c_0$ . For elements that were below the detection limit in the initial magnetite,  $c_0$  was set to 0. The difference in log  $D$  between that calculated using the limit of detection of spot analyses or using  $c_0 = 0$  is less

than 0.005 log units.  $c_0$  for all elements not detectable in Mt-1 prior to annealing are reported as “< dl”.

Copper diffusion was particularly fast, such that even at the furthest distance from the melt reservoir the Cu concentration was greater than the original magnetite (originally below detection limit); it was, therefore, not possible to determine  $D$  values for Cu in some experiments. Similarly, Li diffusion was also fast which meant that it was not possible to determine  $D$  values at  $fO_2 < FMQ + 3$ . As we have pointed out earlier, Si diffusion appears to be sufficiently quick that flat profiles were produced in all experiments, thus it was not possible to determine  $D(Si)$  (Supplementary Fig. S2). This contrasts with Si diffusion in silicates, such as olivine, where Si is one of the slowest diffusing species (Dohmen et al. 2002).

For the 12-h experiments,  $D$  values could be measured for elements with  $-16 < \log D < -11.6$ . However,  $D$  values are most accurate for those in the middle of this range where the diffusion distance was not too short (< 12 microns) or too long (e.g. > 600 microns), in which case the diffusion profile appears flat (Supplementary Fig. S2). It was not possible to determine accurate  $D$  values for W and Th at  $fO_2 > FMQ + 1$ , where these elements were particularly incompatible.

Although there were difficulties determining  $K(Zn)$  and  $K(In)$ , it was possible to determine  $D$  values for these elements. Zinc was substantially lost from the melt during experimental runs so that diffusion profiles could be fitted for diffusion out of the magnetite into the melt. Indium was present in the initial magnetite crystal at low concentrations so diffusion still occurred from the melt into the crystal. In some cases there was evidence for a change in the interface concentration, thought to be due to progressive loss of the elements from the melt during runs (Fig. 7). In cases where this occurred, the diffusion profile was only fitted for the initial part of the profile and so the results should be viewed with caution.

### Time-independent diffusion coefficients

Experiments MB-9, MB-3 and MB-2 were conducted over the same  $fO_2$  and  $T$  conditions (FMQ + 2/1150 °C), but MB-9 was annealed for 66.9 h, MB-3 was annealed for 12.0 h, and MB-2 for 161.4 h. Despite the different experiment durations, diffusion coefficients from the three experiments are in agreement within 2 standard deviations (Fig. 8). This shows that diffusion coefficients are independent of experiment duration. Furthermore, the comparison shows no evidence that the 12 h run returns erroneously high diffusivities due to neglect of the ramp time, apart from Zn, which is volatile. Zinc was lost from the melt during the experiment so that it was the only cation observed with diffusion consistently out of the magnetite bucket. It is possible that during the shortest experimental duration there may have been

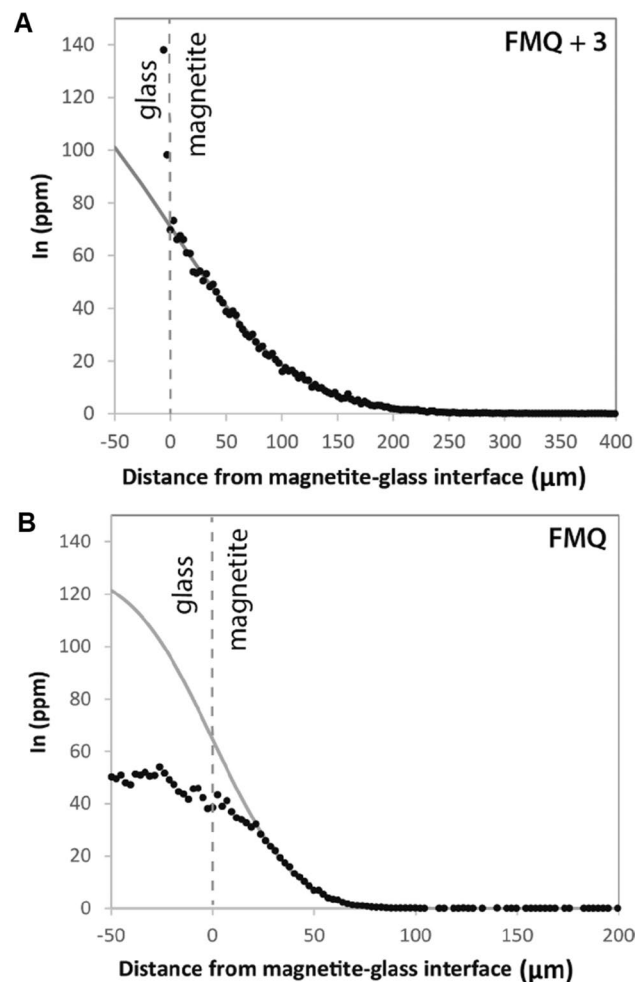


**Fig. 7** Analytical traverse for indium in **a** experiment MB-21 (FMQ) and **b** MB-14 (FMQ + 3). Indium is progressively lost, presumed due to volatility, at lower  $fO_2$  (**b**). The diffusion profile and diffusion coefficient were calculated only for the start of the profile prior to substantial volatile loss. Indium volatility does not appear to pose a problem at higher  $fO_2$  (**a**)

enough Zn in the melt early on so that there was also some diffusion in, resulting in a slower net diffusion rate (Supplementary Table S1). Some elements, e.g. Mo, not added to the MB-3 starting composition, were added to the starting composition used in MB-9, so  $K$  and  $D$  values for Mo could only be derived from this experiment. Furthermore,  $K$  and  $D$  values for some faster diffusing elements could not be derived from MB-9 because their concentrations were raised above the original concentrations for the whole crystal over the longer experiment durations e.g. U.

### Cation diffusion

As reported in previous work, cation diffusion rates in magnetite exhibit a concave-upwards trend as a function of  $fO_2$ , with a minimum  $D$  at intermediate  $fO_2$ . This is considered to

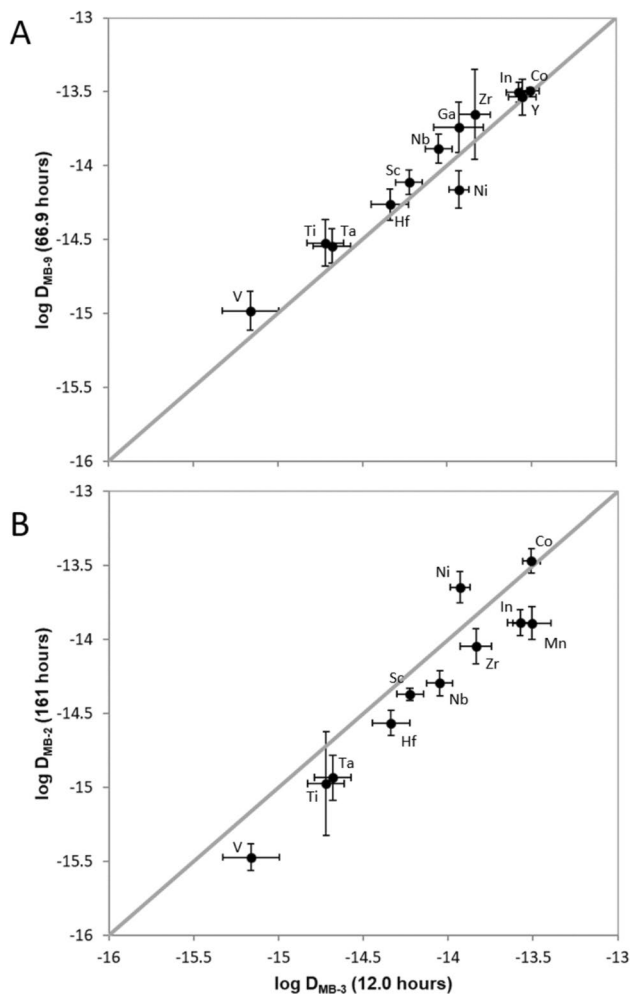


**Fig. 8** Comparison of diffusion coefficients at  $fO_2 = \text{FMQ} + 2$  and  $T = 1150\text{ }^\circ\text{C}$  from experiment at 12.0 h (MB-3) with 66.9 h (MB-9, A) and 161.4 h (MB-2, B) duration for cations which diffused into the magnetite bucket only. Zinc, which diffused out of the magnetite as a result of volatile loss at the start of the experiment, is not plotted. Error bars =  $1\sigma$

be a result of a transition between interstitial- and vacancy-diffusion mechanisms (Lewis et al. 1985). Here, we extend the documentation of this behaviour to  $> 20$  elements. Dieckmann and Schmalzried (1977) derived the following equation to describe the diffusion coefficient for Fe as a function of  $fO_2$ , expressed as a sum of the diffusivities by interstitial and vacancy mechanisms:

$$D_{\text{Fe}} = D_{\text{V}}^0 \exp\left(\frac{-H_{\text{V}}}{RT}\right) a_{\text{O}_2}^{2/3} + D_{\text{I}}^0 \exp\left(\frac{-H_{\text{I}}}{RT}\right) a_{\text{O}_2}^{-2/3} \quad (5)$$

where  $D_{\text{Fe}}$ ,  $D_{\text{V}}$  and  $D_{\text{I}}$  are diffusion coefficients for Fe, vacancy mechanism and interstitial mechanism, respectively,  $H_{\text{V}}$  and  $H_{\text{I}}$  are the activation enthalpy for diffusion by a vacancy and interstitial mechanism, respectively,  $R$  is

ideal gas constant,  $T$  is temperature and  $a_{\text{O}_2}$  is the activity of oxygen. The diffusion of all other cations studied here exhibit a similar behaviour in their response to  $fO_2$  as Fe. Thus, the same equation can also be used to explain cation diffusion for other species. The location of the minimum  $D$  point in  $fO_2 - D$  space varies between the different elements. Using the equation above, curves were fitted to the experimental data for each cation as a function of  $fO_2$  using weighted least square regressions to solve for a vacancy constant ( $D_{\text{V}}^1 = D_{\text{V}}^0 \exp(-H_{\text{V}}/RT)$ ) and an interstitial constant ( $D_{\text{I}}^1 = D_{\text{I}}^0 \exp(-H_{\text{I}}/RT)$ ) with fixed exponents of  $fO_2$  as  $2/3$  and  $-2/3$  for the vacancy and interstitialcy terms, respectively. These fits take account of the errors in  $D$  (Supplementary Table S1); Fig. 6d compares the fits for Sc, which has small errors in  $\log D$ , and Cr, which has more significant errors in  $\log D$ . The fit of the data to Eq. 5 is excellent for most elements. For certain elements, such as In and Zn, the fit is less good, perhaps accounted for by the volatility problem noted earlier. The fit of the data is also less good for some polyvalent cations, such as U, and elements for which there are fewer data, such as Ti, where exsolution was a problem. Values for  $D_{\text{V}}^1$  and  $D_{\text{I}}^1$ , as well as the minimum  $\log D$  value ( $\log D_{\text{x}}(\text{min})$ ) and  $\log fO_2$  at the minimum in the curve ( $\log fO_2(\text{min})$ ), are given in Table 5.

### Comparison with previous work

The diffusion coefficients for Co, Mn, Cr, Al, Ni and Ti in magnetite as a function of  $fO_2$  have been studied previously at  $1200\text{ }^\circ\text{C}$  (Dieckmann et al. 1978; Dieckmann and Schmalzried 1986; Aggarwal and Dieckmann 2002). However, the majority of existing work has employed a different experimental technique using radioactive tracers—such as Fe-59, Ti-44 and Co-60—dropped in the form of aqueous solutions onto a polished disk of magnetite (e.g. Aggarwal and Dieckmann 2002; Lu and Dieckmann 1992). This work included evaluation of the diffusivity of Fe in magnetite as a function of temperature. Assuming the relationship between temperature and the diffusion coefficients of other cations is the same as for Fe, it is possible to predict the diffusion coefficients for the other cations at  $1150\text{ }^\circ\text{C}$  so that they can be more readily compared to this dataset. Using this approach for Mn and Ti, the diffusion coefficients derived here are found to agree very well with those predicted from the existing literature data (Supplementary Fig. S3).

The minimum  $\log D$  ( $\log D_{\text{min}}$ ) varies significantly between the different elements in the order  $\text{Cr} < \text{Mo} \approx \text{Ta} < \text{V} < \text{Ti} < \text{Al} < \text{Hf} \approx \text{Nb} < \text{Sc} \approx \text{Zr} - 90 \approx \text{Ga} < \text{In} < \text{Zr} - 92 < \text{Lu} \approx \text{Y} < \text{Ni} < \text{U} \approx \text{Zn} < \text{Mn} \approx \text{Mg} < \text{Co}$ . If our observations of Si have been interpreted correctly, Si would be the fastest diffusing cation from its flat diffusion profiles. Lithium and Cu can also be inferred to be particularly fast diffusing cations, and because of this it was



**Table 5** Values of  $D_v^1$ ,  $D_1^1$ , minimum  $\log f_{O_2}$  and  $D$  of fit to Eq. 5, and various physical parameters for cations in magnetite

Element	Charge	VI Radii ( $\text{\AA}$ ) <sup>a</sup>	Mass (g/mol)	OSPE (KJ) <sup>b</sup>	Electronegativity (Pauling)	Charge density	K (FMQ-1) <sup>c</sup>	K (FMQ+4.89) <sup>c</sup>	$\log Dv^1$ (0.67) <sup>d</sup>	$\log D_1^1$ (-0.67) <sup>d</sup>	Minimum $\log f_{O_2}^e$	Minimum $\log D^e$
Li	1	0.76	6.94			0.544	-	0.216	-	-	-	-
Cu	1	0.77	63.5			0.523	-	0.676	-	-	-	-
Mn	2	0.83	54.9	45.0	1.83	0.835	0.241	1.08	-9.07	-18.8	-7.22	-13.61
Co	2	0.65	58.9	20.0	1.91	1.74	0.935	4.50	-9.13	-18.4	-6.94	-13.47
Ni	2	0.56	58.7	-28.0	1.90	2.72	3.01	18.4	-9.68	-18.5	-6.58	-13.79
Mg	2	0.72	24.3	20.0	1.31	1.28	0.204	0.660	-9.27	-18.5	-6.87	-13.58
Zn	2	0.74	65.4	53.0	1.81	1.18	0.667	1.77	-9.18	-18.8	-7.20	-13.71
Sc	3	0.745	45.0		1.54	1.73	0.753	0.119	-9.60	-20.2	-7.91	-14.60
Al	3	0.535	27.0	-36.0	1.61	4.68	1.05	0.112	-10.3	-21.0	-8.01	-15.33
Ga	3	0.62	69.7	-4.00	2.01	3.01	2.79	0.318	-9.48	-20.3	-8.07	-14.58
In	3	0.8	115		1.69	1.40	1.30	0.00199	-8.97	-20.1	-8.28	-14.22
Y	3	0.9	88.9		0.950	0.982	0.00257	0.000506	-9.04	-19.6	-7.89	-14.03
Cr	3	0.615	52.0	-160	1.55	3.08	234	45.9	-12.0	-21.6	-7.18	-16.47
Lu	3	0.861	175		1.25	1.12	0.00981	0.00207	-9.15	-19.6	-7.81	-14.07
V	3	0.78	50.9	-55.0	1.90	1.51	17.5	0.110	-10.5	-21.2	-7.94	-15.56
Si	4	0.4	28.1		1.90	14.9	0.0066	0.0045	-	-	-	-
Ti	4	0.605	47.9	50.0	1.63	4.31	4.97	0.224	-10.1	-21.3	-8.40	-15.41
V	4	0.58	50.9		1.66	4.89	17.5	0.110	-10.5	-21.2	-7.94	-15.56
Zr	4	0.72	91.2		1.22	2.56	0.304	0.00628	-9.17	-20.6	-8.56	-14.60
Hf	4	0.71	178		1.30	2.67	0.497	0.00725	-9.86	-21.1	-8.40	-15.18
U	4	0.89	238		1.30	1.35	0.00677	0.0000904	-8.23	-19.8	-8.63	-13.71
Nb	5	0.64	92.9		1.33	4.55	0.519	0.00235	-9.50	-21.4	-8.90	-15.17
Ta	5	0.64	181		1.27	4.55	0.334	0.00241	-10.3	-22.0	-8.77	-15.87
Mo	6	0.59	95.9		1.60	6.97	2.77	0.000520	-10.3	-22.2	-8.89	-15.91
W	6	0.6	184		1.30	6.63	0.0238	-	-	-	-	-

<sup>a</sup>Ionic radii from Shannon (1976)

<sup>b</sup>Octahedral site preference energy from O'Neill and Navrotsky (1984)

<sup>c</sup>Magnetite-melt partition coefficients from this study (Supplementary Table S1)

<sup>d</sup> $D_v^1 = D_0 \exp(-H_v/RT)$  and  $D_1^1 = D_1 \exp(-H_1/RT)$  with fixed exponents of  $f_{O_2}$  as 2/3 and -2/3 following Eq. 5

<sup>e</sup>Minimum  $\log f_{O_2}$  and  $\log D$  are location of minimum in  $\log f_{O_2}$ - $D$  space of fit to Eq. 5

only possible to quantify Li and Cu diffusion rates in the two experiments at the highest  $fO_2$  conditions (FMQ + 3 and + 4.89).

The location of the  $\log D_{\min}$  in  $fO_2$  space describes the preference of different cations for a vacancy versus an interstitial mechanism of diffusion. The lower the  $fO_2$  of the minimum  $\log D$ , the greater the preference for a vacancy mechanism over an interstitial mechanism. This preference increases in the order: Nb  $\approx$  Mo < Ta < U < Zr-90  $\approx$  Zr-92 < Hf  $\approx$  Ti < In < Ga  $\approx$  Al < V < Sc  $\approx$  Y < Lu < Mn  $\approx$  Zn  $\approx$  Cr < Co < Mg  $\approx$  Ni. Given that it was only possible to measure  $D$  values for Li and Cu at  $fO_2 = \text{FMQ} + 3$  and + 4.89, it can be inferred that the preference for an interstitial

over vacancy mechanism of diffusion is greatest for these elements. It is worth noting that at the highest  $fO_2$  studied, where the vacancy mechanism dominates, there is a convergence of  $D$  values. At the lowest  $fO_2$ , where the interstitial mechanism is dominant, there is more spread in the  $D$  values for the different cations.

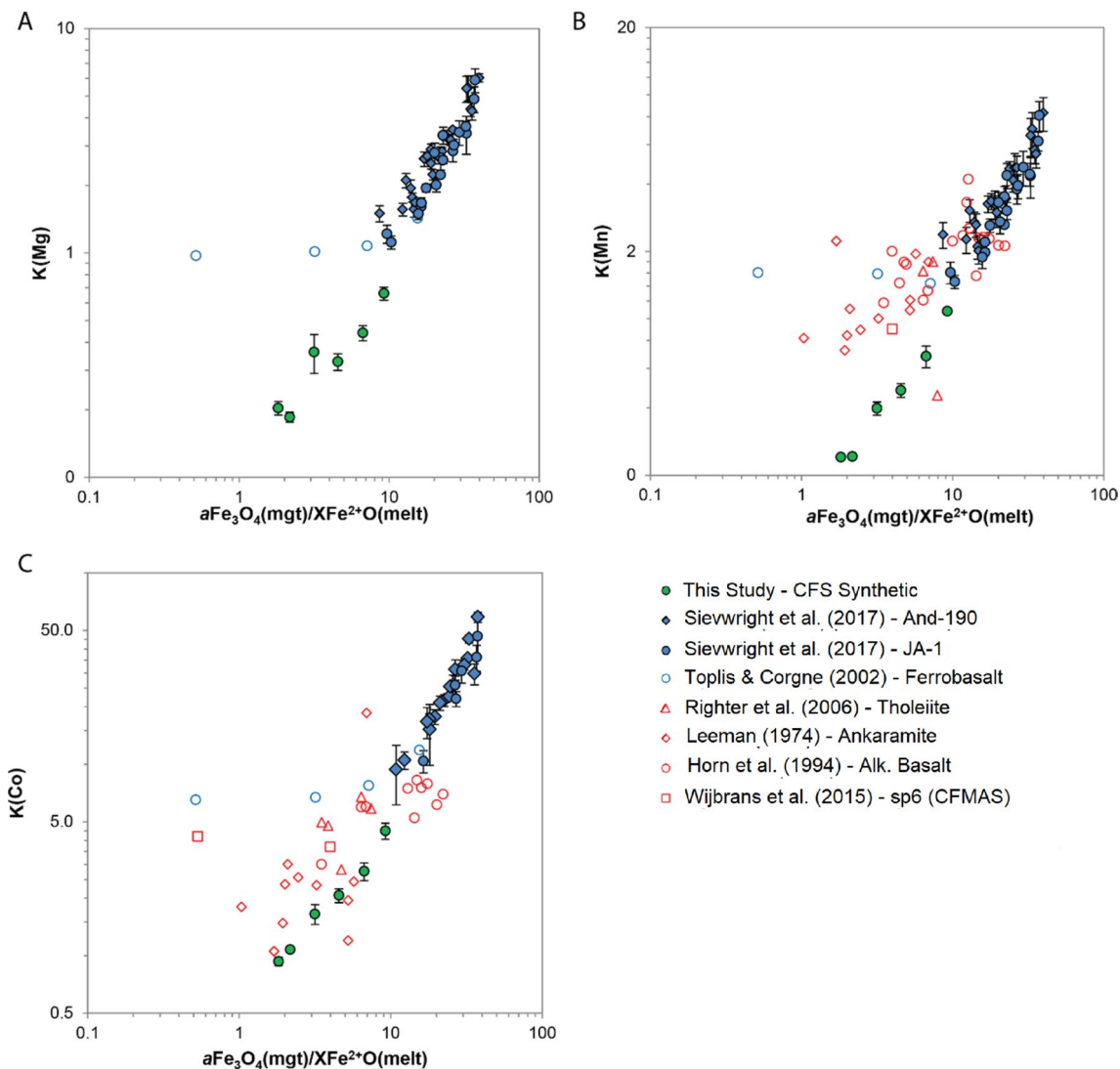


**Fig. 9** Magnetite-melt partition coefficients of **a** Mg, **b** Mn and **c** Co plotted against  $a\text{Fe}_3\text{O}_4(\text{mgt})/X\text{Fe}^{2+}\text{O}(\text{melt})$ .  $a\text{Fe}_3\text{O}_4(\text{mgt})$  approximated using model by O'Neill (1987) with mole fraction on a single cation basis.  $X\text{Fe}^{2+}\text{O}(\text{melt})$  and  $X\text{Fe}^{3+}\text{O}_{1.5}(\text{melt})$  calculated from values approximated using Kress and Carmichael (1991). Literature data

includes: Sievwright et al. (2017) (And -190 and JA-1), Toplis and Corgne (2002) which were conducted at 1068 °C; and Righter et al. (2006), Leeman (1974), Horn et al. (1994) and Wijbrans et al. (2015) which were conducted between 1150 and 1370 °C. Error bars =  $1\sigma$

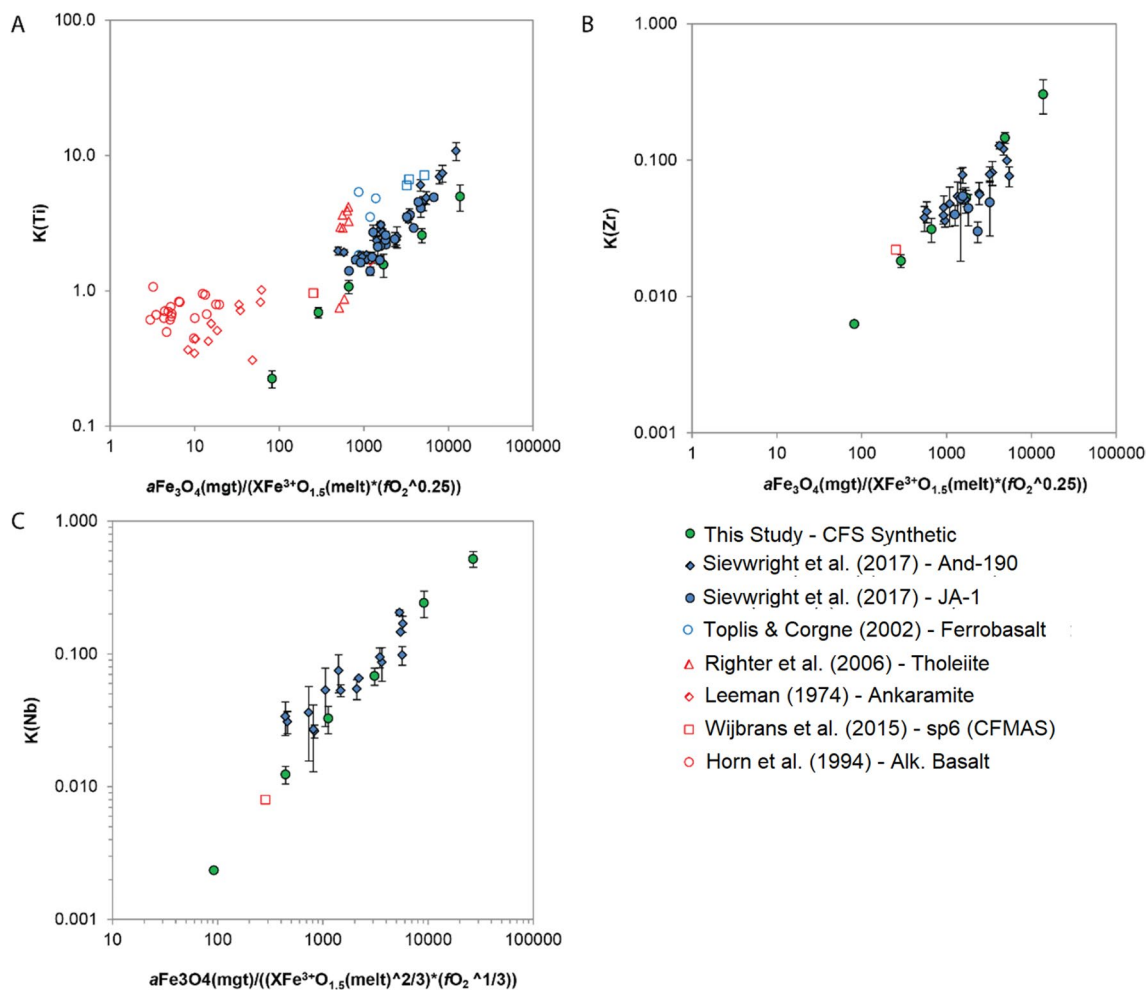


**Fig. 10** Magnetite-melt partition coefficients of **a** Ti and **b** Zr plotted against  $a\text{Fe}_3\text{O}_4^{0.5}/\text{XFeO}_{1.5}$  and **c**  $D(\text{Nb})$  vs.  $a\text{Fe}_3\text{O}_4(\text{mgt})/(\text{XFe}^{3+}\text{O}_{1.5}(\text{melt})^{2/3}) * f\text{O}_2^{(1/3)}$ .  $a\text{Fe}_3\text{O}_4(\text{mgt})$  approximated using model by O'Neill and Wall (1987), with mole fraction on a single cation basis.  $\text{XFe}^{2+}\text{O}(\text{melt})$  and  $\text{XFe}^{3+}\text{O}_{1.5}(\text{melt})$  calculated from values approximated using Kress and Carmichael (1991).

## Discussion

### Controls on magnetite-melt partitioning

Magnetite–melt partition coefficients can be predicted using linear correlations with functions related to  $a\text{Fe}_3\text{O}_4(\text{spinel})$ ,  $\text{XFe}^{2+}\text{O}(\text{melt})$ ,  $\text{XFe}^{3+}\text{O}_{1.5}(\text{melt})$  and  $f\text{O}_2$  (Siewwright et al. 2017). The results here agree with the linear trends defined by Sievwright et al. (2017) for the divalent, tetravalent and pentavalent cations (Figs. 9, 10, 11). A linear trend is also observed for  $K(\text{Sc})$  as a function of  $a\text{Fe}_3\text{O}_4^{0.5}/\text{XFeO}_{1.5}$  which is supported by data from Wijbrans et al. (2015) (Fig. 11b); this suggests that the partitioning of Sc is principally governed by thermodynamic equilibria associated with changes in spinel and melt composition and that there are not substantial changes in the activity coefficients, either in the

Literature data includes: Sievwright et al. (2017) (And -190 and JA-1), Toplis and Corgne (2002), Toplis et al. (1994) which were conducted at 1068 °C; and Righter et al. (2006), Leeman (1974), Horn et al. (1994) and Wijbrans et al. (2015) which were conducted between 1150 and 1370 °C. Error bars =  $1\sigma$

spinel or melt, with changes in bulk composition. The partitioning of Al, however, is different. Whereas there is a weak negative correlation between  $K(\text{Al})$  and  $a\text{Fe}_3\text{O}_4^{0.5}/\text{XFeO}_{1.5}$  in an andesitic to dacitic bulk system, in these experiments there is a positive non-linear correlation (Fig. 11a). It is important to note that, unlike most natural silicate melts, Al is not a major network-forming component of the melt in the experiments reported here so that it is likely that the activity–composition relations in natural silicate melts differ significantly. Alternatively, the partitioning of Al could be more sensitive to spinel composition (e.g. Al content) than other cations studied, possibly because of modification of the activity coefficients in spinel. In these experiments, however, with low-Al spinel,  $K(\text{Al})$  is similar to the other trivalent cations and is dominantly dictated by thermodynamic equilibria between magnetite and melt species.

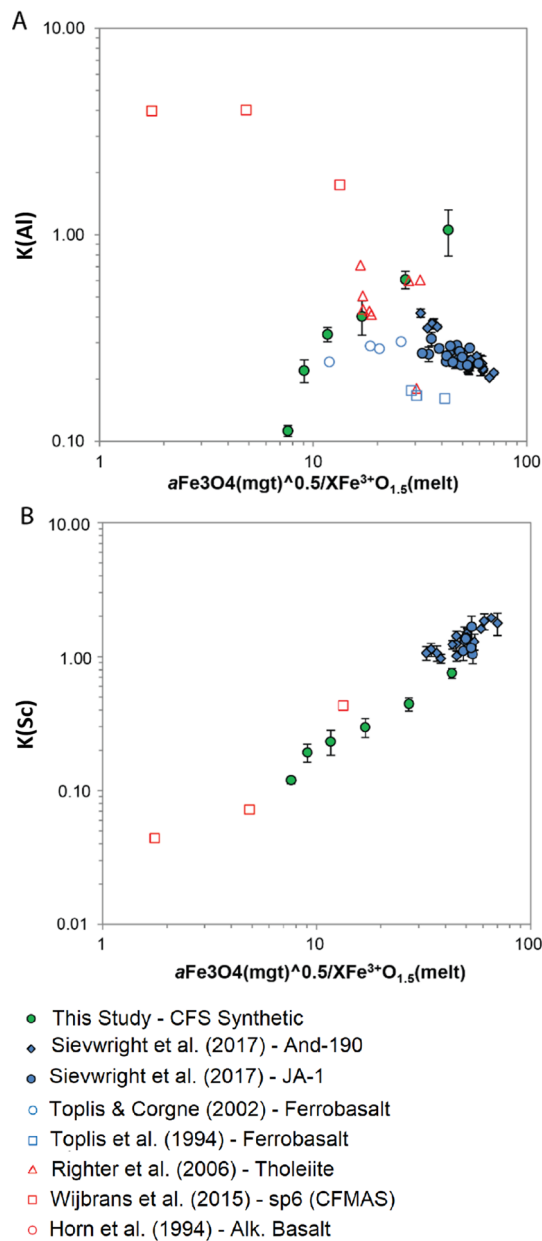


**Fig. 11** Magnetite–melt partition coefficients of **a** Al and **b** Sc plotted against  $a\text{Fe}_3\text{O}_4(\text{mgt})^{0.5}/X\text{Fe}^{3+}\text{O}_{1.5}(\text{melt})$  approximated using model by O'Neill (1987), with mole fraction on a single cation basis.  $X\text{Fe}^{2+}\text{O}(\text{melt})$  and  $X\text{Fe}^{3+}\text{O}_{1.5}(\text{melt})$  calculated from values approximated using Kress and Carmichael (1991). Literature data includes: Siewwright et al. (2017) (And -190 and JA-1), Toplis and Corgne (2002), Toplis et al. (1994), Righter et al. (2006) and Wijbrans et al. (2015). Error bars =  $1\sigma$

### Lattice strain models

The logarithm of partition coefficients plotted vs. ionic radius produces parabolic trends for suites of elements grouped by different valence states (Fig. 12). The apices of these parabolic trends—known as Onuma diagrams (Onuma

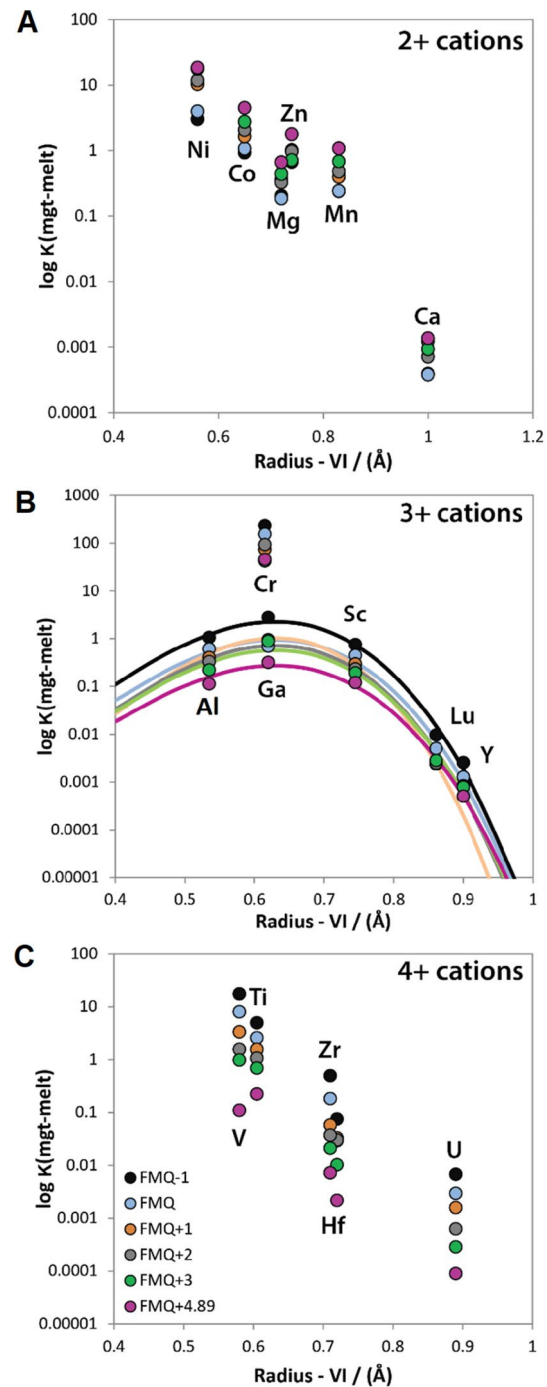


**Fig. 12** Magnetite–melt partition coefficients of **a** divalent, **b** trivalent and **c** tetravalent cations as a function of ionic radius for this as a function of  $f\text{O}_2$ . The solid lines represent fit of trivalent cations to Eq. 6 taken from Blundy and Wood (1994). The optimum radius was fixed to be  $0.63 \text{ \AA}$

et al. 1968)—display the optimal size of the crystal site into which the cations substitute and the curvature indicate the elasticity of the surrounding lattice (Blundy and Wood 1994). In magnetite, both divalent and trivalent cations can



**Table 6** Approximated values of  $E$  and  $K_0$  as a function of  $fO_2$  for the trivalent cations (excluding Cr) using linear trends produced by plotting Eq. 6 assuming they are incorporated into the octahedral site

Parameter	FMQ-1	FMQ	FMQ+1	FMQ+2	FMQ+3	FMQ+4.89
$E$ (GPa)	353.8	340.7	426.8	358.1	345.2	314.3
$K_0$	2.24	0.94	1.02	0.71	0.57	0.27

occupy both the octahedral (B) or tetrahedral (A) sites, with site distributions dependent on temperature according to the octahedral site preference energies of the cations relative to those of  $Fe^{2+}$  and  $Fe^{3+}$  (O'Neill and Navrotsky 1984). Here we have used octahedral radii to represent the data. For the divalent and tetravalent cations, only the right-hand limb of the parabola is evident. The data for V have been included in the plot for the 4+ cations in Fig. 12c, although this cation is present as both 3+ and 4+ in magnetite (O'Neill and Navrotsky 1984; Sievwright et al. 2017) and may be present as 3+, 4+ and 5+ in the melt, depending on  $fO_2$  (e.g. Canil 1999; Mallmann and O'Neill 2009). The very much lower value of  $K(V)$  in the most oxidized experiment (MB-23 at FMQ+4.9) is consistent with a substantial fraction of  $V^{5+}$  in the melt. Likewise, U has also been included with the tetravalent cations, although this element exists as 4+, 5+ and 6+ in silicate melts depending on  $fO_2$  (Halse 2014), and might also have variable oxidation states in  $Fe_3O_4$ , due to electron exchange reactions ( $Fe^{3+} + U^{4+} = Fe^{2+} + U^{5+}$  and/or  $2 Fe^{3+} + U^{4+} = 2 Fe^{2+} + U^{6+}$ ). The smaller  $U^{5+}$  and  $U^{6+}$  cations may fit more comfortably into the spinel crystal structure of  $Fe_3O_4$  than the large  $U^{4+}$  cation.

Some elements do not fit onto the parabolic trend for partition coefficients as a function of ionic radius in octahedral coordination. For example, Cr has a much higher partition coefficient than would be expected based on the parabolic fit defined by the other trivalent cations. The other trivalent cations produce a well-defined parabola with a peak at approximately  $0.63 \text{ \AA}$ , suggesting this is the optimal trivalent site radius ( $r_O$ ). The lattice-strain model for the partition coefficient  $K_i$  of a homovalent cation  $i$  depends on the difference between the ionic radius of the cation ( $r_i$ ) and  $r_O$ , and the Young's modulus ( $E$ ) of the host crystal:

$$\ln K_i = \ln K_0 - \frac{4\pi EN_A}{RT} \left( \frac{r_i}{3} + \frac{r_0}{6} \right) (r_i - r_O)^2 \quad (6)$$

where  $N_A$  is Avogadro's number and  $K_0$  is the hypothetical partition coefficients of a cation with an optimal radius for the site (Blundy and Wood 1994). The partition coefficients for the trivalent cations (excluding  $Cr^{3+}$  because of this cation's large crystal field effects) can be plotted according to Eq. 6 using the suggested  $r_0$  of  $0.63 \text{ \AA}$ . This produces straight lines from which both  $E$  and  $K_0$  can be approximated as a function of  $fO_2$  for these experiments. Using the identified  $K_0$ ,  $E$  and  $r_0$  values, parabolic trends can be drawn which

can be used to predict  $K$  as a function of ionic radius. These fits are shown as a function of  $fO_2$  in Fig. 12b and values of  $E$  and  $K_0$  are provided in Table 6. Lattice strain models were not fitted to the divalent and tetravalent cations because only the right limb of the Onuma diagram was apparent and due to the possible mixed-valence states for some elements.

### Diffusion in magnetite as a function of $fO_2$

In the experiments reported here, Li and Cu diffused rapidly such that it was only possible to calculate  $D$  values for these elements at  $fO_2 > FMQ + 2$ . Copper and Li diffusion have been observed to be quick relative to higher valence cations in other minerals (e.g. Seo and Heinrich 2013). The ionic radius of  $Cu^+$  and  $Li^+$  are close to the middle of the range of other cations studied but their common property is their univalent state, which gives them a very low charge/radius ratio. It is plausible that Cu diffusion was only measurable at  $fO_2 > FMQ + 2$  as a result of the increased abundance of  $Cu^{2+}$ , which would be expected to diffuse slower than  $Cu^+$ . Similar to Cu and Li, Si diffusion was particularly fast such that it was not possible to interpret  $D$  values at any  $fO_2$  studied. In comparison to all other cations studied, Si has the smallest ionic radius ( $0.4 \text{ \AA}$  for  $Si^{4+}$  in VI coordination; Shannon 1976), which suggests that this could be important in permitting such rapid diffusion. Niobium and Ta have identical charge and similar partition coefficients, but there has been considerable debate as to whether Nb and Ta have the same cationic radius. Given their differing rates of diffusion presented here, these results could support that the cationic radius of Nb and Ta may differ in magnetite, as has been suggested to be the case in amphibole (e.g. Tiepolo et al. 2000; Nandedkar et al. 2016).

To assess the relative controls of different parameters on the vacancy and interstitialcy diffusion mechanisms identified, values for the vacancy constant ( $D_V^1 = D_V \exp(-H_V/RT)$ ) and the interstitial constant ( $D_I^1 = D_I \exp(-H_I/RT)$ ) from Eq. 5 were studied separately. The following parameters were investigated: ionic radius (Shannon 1976), charge density,  $K_M$  (reported here), site preference energy (O'Neill and Navrotsky 1984), electronegativity, charge and atomic mass.

The values of  $\log D_V^1$  mostly vary less than those for  $\log D_I^1$ , with all values ranging between  $-10.5$  and  $-8.97$  apart from U and Cr. There is an increase in  $\log D_V^1$  with increasing ionic radius and decreasing charge density for

most cations with the exception of Cr and U (Supplementary Fig. S4). The observed relationship could be a result of cations with higher charge density having stronger interactions and forming stronger bonds with surrounding oxygen anions so that they cannot jump between vacant sites as easily by a vacancy mechanism. The multiple possible valence states of U could explain why it does not fit on this trend.  $\log D_V^1$  was also plotted against  $K$  at  $fO_2 = FMQ + 4.89$  (most oxidising condition studied where the vacancy mechanism is most dominant); this produced a negative correlation excluding the 2+ cations, suggesting  $K$  could exert some control on vacancy diffusion (Supplementary Fig. S4). It is important to note that this correlation aids in explaining the slower diffusion rate for Cr. The fact that the 2+ cations do not appear to follow this relationship could reflect their higher affinity for interstitialcy diffusion (which might be less influenced by  $K$ ) in comparison to higher valence cations. Site preference energies were determined for some cations in oxide spinels, relative to  $Fe^{3+}$  as a zero reference point (O'Neill and Navrotsky, 1984). Cations with a greater affinity for octahedral coordination have a more negative site preference energy. There is a trend of increasing  $\log D_V^1$  with increasing site preference energy for 2+ and 3+ cations (Supplementary Fig. S4), indicating that cations with a greater affinity for octahedral coordination diffuse slower by a vacancy mechanism. No significant relationship is evident between  $D_V^1$  and ionic charge (Supplementary Fig. S4) and no trend for  $\log D_V^1$  was found as a function of electronegativity or atomic mass.

There is generally more variation in values in  $\log D_I^1$  for the majority of cations. This means that interstitialcy diffusion can usually reach faster rates than vacancy diffusion. For all except the 2+ cations, there is a general increase in  $\log D_I^1$  with increasing ionic radius and decreasing charge density (Supplementary Fig. S5), although the latter trend is more scattered than that defined by  $\log D_V^1$  and varies over a greater range from  $-22.2$  to  $-19.6$ . There is a relatively well-defined linear trend for the trivalent and tetravalent cations as a function of  $K$  at  $fO_2 = FMQ - 1$  (most reducing condition where interstitialcy mechanism is most dominant), however, the 2+, 5 and 6+ cations sit off this trend (Supplementary Fig. S5). Unlike  $\log D_V^1$ , there is a distinct decrease in  $\log D_I^1$  with increasing ionic charge (Supplementary Fig. S5), which suggests that this parameter is more important in controlling the interstitialcy over the vacancy mechanism of diffusion. No trend for  $\log D_I^1$  was found as a function of electronegativity or atomic mass.

Plotting  $\log D_V^1$  vs.  $\log D_I^1$  allows the preference for a vacancy relative to interstitialcy mechanism of diffusion to be assessed for each cation (Fig. 13). Cations with a higher valence have increased preference for the vacancy over the interstitialcy mechanism of diffusion. Linear arrays can be defined on this plot for the 3+ and higher valence ions

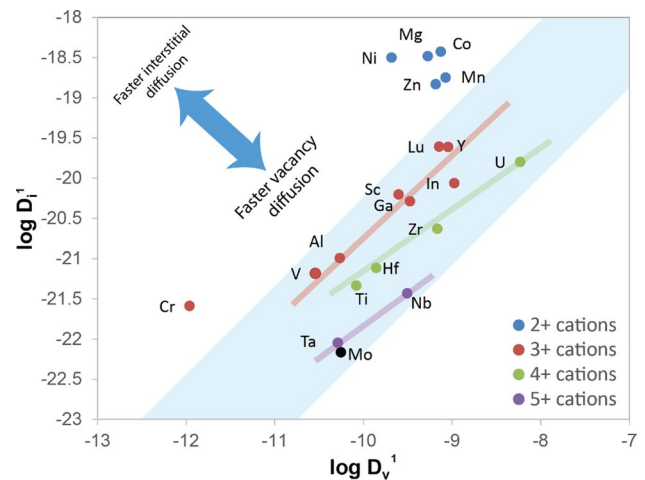


**Fig. 13** The logarithm of  $D_I^1$  ( $D_I^1 = D_i^0 \exp(-H_i/RT)$ ) vs. the logarithm of  $D_V^1$  ( $D_V^1 = D_v^0 \exp(-H_v/RT)$ ) for divalent ( $Mg^{2+}$ ,  $Co^{2+}$ ,  $Mn^{2+}$ ,  $Ni^{2+}$  and  $Zn^{2+}$ ), trivalent ( $Al^{3+}$ ,  $Ga^{3+}$ ,  $Sc^{3+}$ ,  $In^{3+}$ ,  $Y^{3+}$  and  $Lu^{3+}$ ), tetravalent ( $Ti^{4+}$ ,  $Zr^{4+}$ ,  $Hf^{4+}$  and  $U^{4+}$ ), and pentavalent ( $Nb^{5+}$  and  $Ta^{5+}$ ) cations. The data for V are consistent with its oxidation state being 3+. However, the data for Mo suggest a higher oxidation state than 4+

studied, apart from Cr. The deviation in the behaviour of Cr could be explained by its higher  $K$  value and/or increased preference for octahedral coordination relative to the other trivalent cations studied. Vanadium plots along the trend defined by the trivalent cations, which supports the inference that  $V^{3+}$  is the predominant diffusing species in magnetite, at least under the experimental conditions considered. The divalent cations form a cluster offset from the trend defined by the other cations, possibly as a result of their lower charge. Within the divalent cations, those cations, which plot furthest from the dominant linear array have strongest preference for octahedral coordination.

In conclusion, the mechanism of diffusion is primarily controlled by the concentration of interstitials relative to vacancies in the lattice, which is a function of  $fO_2$  (Eq. 5). The preference for interstitialcy diffusion and its rate decrease with ionic charge (Supplementary Fig. S5). Cations with greater preference for octahedral coordination also have an increased affinity for an interstitialcy over a vacancy mechanism of diffusion (Fig. 13). Vacancy diffusion, however, is predominantly controlled by charge density and secondarily by the partition coefficient (which could express how well an element fits into cation sites in the lattice) and crystal-field site preference energy. Cations with a higher charge density, lower mineral-melt partition coefficient, and higher preference for octahedral coordination diffuse more slowly by the vacancy mechanism. These factors do not exert as strong an influence on the rate of interstitial-mediated diffusion in the low  $fO_2$  regime.

## Implications for studying natural systems

### Diffusion coefficients

Diffusion modelling of chemical gradients in minerals is frequently applied as a chronological tool to constrain the timescales of geological processes. Diffusion speedometry requires optimal thermal histories and diffusion rates to produce a measurable diffusion gradient. Mercer et al. (2015) applied diffusion modelling of Ti gradients in quartz to investigate the formation and cooling time scales of quartz from porphyry dyke intrusions and hydrothermal veins associated with porphyry copper mineralisation. A calibration was developed to measure Ti gradients in quartz using high spatial resolution SEM cathodoluminescence images over distances as short as 2  $\mu\text{m}$ . Cation diffusion is significantly faster in magnetite than silicate minerals such as quartz (typically more than 4 orders of magnitude). As a result, diffusion gradients in magnetite could be amenable to analysis by LA-ICP-MS, even at temperatures relevant for the magmatic-hydrothermal transition (e.g. 700  $^{\circ}\text{C}$ ), generating broader diffusion profiles for a range of elements, which would not be easily detectable in minerals with slower diffusion. On the other hand, magnetite may not be so well suited for tracking the timescales of higher temperature magmatic processes, where rapid diffusion is likely to generate flat, completely relaxed diffusion profiles. Owing to its cubic symmetry, magnetite does not exhibit variation in diffusivity with crystallographic orientation, thereby removing an additional aspect of complication in using magnetite for diffusion speedometry relative to anisotropic phases. The diffusion rates of various trace elements in magnetite cover nearly four orders of magnitude, offering a range of possible elements to cross-check the timescales of processes.

The trace element contents of natural hydrothermal magnetite are often heterogeneous on the grain scale (Cook et al. 2016), sometimes exhibiting oscillatory zoning (e.g. Knipping et al. 2015). Copper commonly exhibits a remarkable scale of heterogeneity in natural magnetite, which has been dismissed by some as a result of ‘nanoinclusions’ (e.g. Hough et al. 2008), however, it is possible that this heterogeneity could also be explained by the rapid diffusion of Cu. Nevertheless, it is important to consider that the heterogeneous chemistry on the grain scale may not be solely a result of diffusion processes, but instead a result of dissolution-precipitation processes (e.g. Hu et al. 2015).

### Magnetite-melt partition coefficients

Experiments conducted here provide partition coefficients for a number of elements, such as Mo, U, W, Y, Lu and

Li, which until now have not been investigated comprehensively. Magnetite-melt partitioning for most elements can be explained in terms of changes in  $f\text{O}_2$  and melt composition. The latter may result in changes in the activity coefficients in the melt with variations in the major element composition of the system (Siewwright et al. 2017), an effect that is particularly strong for Al and Ga.

## Conclusions

Diffusion coefficients ( $D$ ) for a wide range of cations in magnetite vary over 4 orders of magnitude. Diffusion coefficients at a given  $f\text{O}_2$  generally increase in the order:  $\text{Cr} < \text{Mo} \approx \text{Ta} < \text{V} < \text{Ti} < \text{Al} < \text{Hf} \approx \text{Nb} < \text{Sc} \approx \text{Zr} \approx \text{Ga} < \text{In} < \text{Lu} \approx \text{Y} < \text{Ni} < \text{U} \approx \text{Zn} < \text{Mn} \approx \text{Mg} < \text{Co} < \text{Li} < \text{Cu}$ . Thus, Cu contents of magnetites are most susceptible to diffusive re-equilibration whereas the original content of slow diffusing elements, such as Cr, should be best preserved. Plots of  $\log D$  as a function of  $\log f\text{O}_2$  produce V-shaped trends for all the investigated elements, representing two different mechanisms of diffusion that depend on  $(f\text{O}_2)^{-2/3}$  and  $(f\text{O}_2)^{2/3}$ , probably interstitialcy and vacancy mechanisms respectively. The preference for interstitialcy diffusion relative to vacancy diffusion is primarily controlled by the concentration of interstitials relative to vacancies in the lattice which is dictated by  $f\text{O}_2$  via  $3 \text{Fe}^{2+} + 2/3 \text{O}_2 \leftrightarrow 2 \text{Fe}^{3+} + \text{V}_{\text{Fe}} + 1/3 \text{Fe}_3\text{O}_4$ . The minimum of the V-shaped trends in  $\log D - \log f\text{O}_2$  space differs for the various cations. Lower valence cations have greater preference and rate of interstitialcy diffusion. Cations with higher charge density, lower magnetite-melt partition coefficients, and a higher preference for octahedral coordination diffuse at a slower rate by a vacancy mechanism.

Magnetite-melt partitioning can be explained by thermodynamic equilibria between magnetite and melt associated with changing  $a\text{Fe}_3\text{O}_4(\text{spinel})$ ,  $X\text{Fe}^{2+}\text{O}(\text{melt})$ ,  $X\text{Fe}^{3+}\text{O}_{1.5}(\text{melt})$  and  $f\text{O}_2$ . These thermodynamic relationships can be used to explain partitioning of a number of elements, which until now have not been investigated comprehensively as a function of  $f\text{O}_2$ . Nevertheless, for some elements, these relationships break down for spinel compositions containing lower fractions of  $\text{Fe}_3\text{O}_4$  than those studied here and for different bulk compositions. This could be related to changing activity-composition relations in either the spinel or in the melt.

The new partitioning and diffusion parameters reported here open up new possibilities for constraining the oxidation state and chemistry of silicate melts, as well as scope for

determining the duration of late magmatic and hydrothermal phenomena.

**Acknowledgements** This work was financially supported by the Imperial President's PhD Scholarship Scheme, IOM<sup>3</sup> and the Australian Bicentennial Scholarship. Dean Scott provided assistance when preparing magnetite crucibles for experiments. Clara Wilkinson kindly donated the crystals of magnetite (Mt-1) which were used in the experiments. John Spratt is thanked for help with EPMA, and Mike Jollands, Will Brownscombe, Elly Harman, and Clara Wilkinson for assistance with LA-ICP-MS analyses. We are very grateful to James van Orman and Dante Canil for their thorough and thoughtful reviews, which helped improve the quality of this report, as well as Othmar Müntener for his editorial handling.

**Open Access** This article is licensed under a Creative Commons Attribution 4.0 International License, which permits use, sharing, adaptation, distribution and reproduction in any medium or format, as long as you give appropriate credit to the original author(s) and the source, provide a link to the Creative Commons licence, and indicate if changes were made. The images or other third party material in this article are included in the article's Creative Commons licence, unless indicated otherwise in a credit line to the material. If material is not included in the article's Creative Commons licence and your intended use is not permitted by statutory regulation or exceeds the permitted use, you will need to obtain permission directly from the copyright holder. To view a copy of this licence, visit <http://creativecommons.org/licenses/by/4.0/>.

## References

- Abe M, Kawachi M, Nomura S (1972) X-ray and neutron diffraction studies in spinel  $\text{Fe}_2\text{MoO}_4$ . *J Phys Soc Jpn* 33:1296–1302
- Aggarwal S, Dieckmann R (2002) Point defects and cation tracer diffusion in  $(\text{Ti}_x\text{Fe}_{1-x})_{3-8}\text{O}_4$  1. Non-stoichiometry and point defects. *Phys Chem Miner* 29:695–706
- Berry AJ, O'Neill HSC (2004) A XANES determination of the oxidation state of chromium in silicate glasses. *Am Miner* 89:790–798
- Berry AJ, O'Neill HSC, Scott DR, Foran GJ, Shelley JMG (2006) The effect of composition on  $\text{Cr}^{2+}/\text{Cr}^{3+}$  in silicate melts. *Am Miner* 91:11–12
- Blundy J, Wood B (1994) Prediction of crystal-melt partition-coefficients from elastic-moduli. *Nature* 372:452–454
- Canil D (1999) Vanadium partitioning between orthopyroxene, spinel and silicate melt and the redox states of mantle source regions for primary magmas. *Geochim Cosmochim Acta* 63:557–572
- Cook N, Ciobanu CL, George L, Zhu ZY, Wade B, Ehrig K (2016) Trace element analysis of minerals in magmatic-hydrothermal ores by laser ablation inductively-coupled plasma mass spectrometry: approaches and opportunities. *Minerals* 6:111
- Crank J (1975) *The mathematics of diffusion*. Clarendon, Oxford
- Dare SA, Barnes SJ, Beaudoin G (2012) Variation in trace element content of magnetite crystallized from a fractionating sulfide liquid, Sudbury, Canada: Implications for provenance discrimination. *Geochim Cosmochim Acta* 88:27–50
- Dieckmann R (1982) Defects and cation diffusion in magnetite (IV): nonstoichiometry and point defect structure of magnetite ( $\text{Fe}_{3-8}\text{O}_4$ ). *Berichte Bunsengesellschaft Phys Chemie* 86:112–118
- Dieckmann R, Schmalzried H (1977) Defects and cation diffusion in magnetite (I). *Berichte Bunsengesellschaft Phys Chemie* 81:344–347
- Dieckmann R, Schmalzried H (1986) Defects and cation diffusion in magnetite (VI): point defect relaxation and correlation in cation tracer diffusion. *Berichte Bunsengesellschaft Phys Chemie* 90:564–575
- Dieckmann R, Mason TO, Hodge JD, Schmalzried H (1978) Defects and cation diffusion in magnetite (III). Tracer diffusion of foreign tracer cations as a function of temperature and oxygen potential. *Berichte Bunsengesellschaft Phys Chemie* 82:778–783
- Dohmen R, Chakraborty S, Becker HW (2002) Si and O diffusion in olivine and implications for characterizing plastic flow in the mantle. *Geophys Res Lett* 29:1–26
- Halse H (2014) Using synchrotron radiation to determine the oxidation state of uranium in magmas. PhD Thesis, Imperial College, London
- Henderson P, Nolan J, Lowry RK (1986) Cation diffusion in natural silicate melts. *Materials science forum*, vol 7. Trans Tech Publications Ltd., Zurich, pp 257–266
- Holzheid A, Borisov A, Palme H (1994) The effect of oxygen fugacity and temperature on solubilities of nickel, cobalt, and molybdenum in silicate melts. *Geochim Cosmochim Acta* 58:1975–1981
- Horn I, Foley SF, Jackson SE, Jenner GA (1994) Experimentally determined partitioning of high-field strength-elements and selected transition-elements between spinel and basaltic melt. *Chem Geol* 117:193–218
- Hough RM et al (2008) Naturally occurring gold nanoparticles and nanoplates. *Geology* 36:571–574
- Hu H, Lentz D, Li JW, McCarron T, Zhao XF, Hall D (2015) Reequilibration processes in magnetite from iron skarn deposits. *Econ Geol* 110:1–8
- Katsura T, Wakihara M, Hara SI, Sugihara T (1975) Some thermodynamic properties of spinel solid solutions with the  $\text{Fe}_3\text{O}_4$  component. *J Solid State Chem* 13:107–113
- Knipping JL et al (2015) Trace elements in magnetite from massive iron oxide-apatite deposits indicate a combined formation by igneous and magmatic-hydrothermal processes. *Geochim Cosmochim Acta* 171:15–38
- Kress VC, Carmichael IS (1991) The compressibility of silicate liquids containing  $\text{Fe}_2\text{O}_3$  and the effect of composition, temperature, oxygen fugacity and pressure on their redox states. *Contrib Miner Petrol* 108:82–92
- Leeman WP (1974) Experimental determination of the partitioning of divalent cations between olivine and basaltic liquid. PhD Thesis, University of Oregon
- Lewis GV, Catlow CRA, Cormack AN (1985) Defect structure and migration in  $\text{Fe}_3\text{O}_4$ . *J Phys Chem Solids* 46:1227–1233
- Lu FH, Dieckmann R (1992) Point defects and cation tracer diffusion in  $(\text{Co}, \text{Fe}, \text{Mn})_{3-8}\text{O}_4$  spinels: I. Mixed spinels  $(\text{Co}_x\text{Fe}_{2y}\text{Mn}_y)_{3-8}\text{O}_4$ . *Solid State Ionics* 53:290–302
- Mallmann G, O'Neill HSC (2009) The crystal/melt partitioning of V during mantle melting as a function of oxygen fugacity compared with some other elements (Al, P, Ca, Sc, Ti, Cr, Fe, Ga, Y, Zr and Nb). *J Petrol* 50:1765–1794
- Mercer CN, Reed MH, Mercer CM (2015) Time scales of porphyry Cu deposit formation: Insights from titanium diffusion in quartz. *Econ Geol* 110:587–602
- Nadoll P, Angerer T, Mauk JL, French D, Walshe J (2014) The chemistry of hydrothermal magnetite: a review. *Ore Geol Rev* 61:1–32
- Nandedkar RH, Hürlimann N, Ulmer P, Müntener O (2016) Amphibole-melt trace element partitioning of fractionating calc-alkaline magmas in the lower crust: an experimental study. *Contrib Miner Petrol* 171:71
- O'Neill HSC, Navrotsky A (1984) Cation distributions and thermodynamic properties of binary spinel solid solutions. *Am Miner* 69:733–753
- O'Neill HSC (1987) Quartz-fayalite-iron and quartz-fayalite-magnetite equilibria and the free energy of formation of fayalite ( $\text{Fe}_2\text{SiO}_4$ ) and magnetite ( $\text{Fe}_3\text{O}_4$ ). *Am Miner* 72:67–75



- O'Neill HSC (1988) Systems Fe–O and Cu–O; thermodynamic data for the equilibria Fe–“FeO”, Fe–Fe<sub>3</sub>O<sub>4</sub>, “FeO”–Fe<sub>3</sub>O<sub>4</sub>, Fe<sub>3</sub>O<sub>4</sub>–Fe<sub>2</sub>O<sub>3</sub>, Cu–Cu<sub>2</sub>O, and Cu<sub>2</sub>O–CuO from emf measurements. *Am Miner* 73:470–486
- O'Neill HSC, Eggins SM (2002) The effect of melt composition on trace element partitioning: an experimental investigation of the activity coefficients of FeO, NiO, CoO, MoO<sub>2</sub> and MoO<sub>3</sub> in silicate melts. *Chem Geol* 186:151–181
- O'Neill HSC, Berry AJ, Eggins SM (2008) The solubility and oxidation state of tungsten in silicate melts: implications for the comparative chemistry of W and Mo in planetary differentiation processes. *Chem Geol* 255:346–359
- Onuma N, Higuchi H, Wakita H, Nagasawa H (1968) Trace element partition between two pyroxenes and the host lava. *Earth Planet Sci Lett* 5:47–51
- Van Orman JA, Crispin KL (2010) Diffusion in oxides. *Rev Mineral Geochem* 72:757–825
- Prowatke D, Klemme S (2006) Rare earth element partitioning between titanite and silicate melts: Henry's law revisited. *Geochim Cosmochim Acta* 70:4997–5012
- Righter K, Leeman WP, Hervig RL (2006) Partitioning of Ni, Co and V between spinel-structured oxides and silicate melts: importance of spinel composition. *Chem Geol* 227:1–25
- Roeder PL, Reynolds I (1991) Crystallization of chromite and chromium solubility in basaltic melts. *J Petrol* 32:909–934
- Schreiber HD, Haskin LA (1976) Chromium in basalts: experimental determination of redox states and partitioning among synthetic silicate phases. In: Lunar and planetary science conference proceedings, vol 7, pp 1221–1259
- Seo JH, Heinrich CA (2013) Selective copper diffusion into quartz-hosted vapor inclusions: evidence from other host minerals, driving forces, and consequences for Cu–Au ore formation. *Geochim Cosmochim Acta* 113:60–69
- Shannon RD (1976) Revised effective ionic radii and systematic studies of interatomic distances in halides and chalcogenides. *Acta Crystallogr Sect A Cryst Phys Diffract Theor Gener Crystallogr* 32:751–767
- Siewwright RH, Wilkinson JJ, O'Neill HSC, Berry AJ (2017) Thermodynamic controls on element partitioning between titanomagnetite and andesitic–dacitic silicate melts. *Contrib Miner Petrol* 172:62
- Spandler C, O'Neill HSC (2010) Diffusion and partition coefficients of minor and trace elements in San Carlos olivine at 1300 °C with some geochemical implications. *Contrib Miner Petrol* 159:791–818
- Tiepolo M, Vannucci R, Oberti R, Foley S, Bottazzi P, Zanetti A (2000) Nb and Ta incorporation and fractionation in titanian pargasite and kaersutite: crystal–chemical constraints and implications for natural systems. *Earth Planet Sci Lett* 176:185–201
- Toplis MJ, Corgne A (2002) An experimental study of element partitioning between magnetite, clinopyroxene and iron-bearing silicate liquids with particular emphasis on vanadium. *Contrib Miner Petrol* 144:22–37
- Toplis MJ, Libourel G, Carroll MR (1994) The role of phosphorus in crystallization processes of basalt: an experimental—study. *Geochim Cosmochim Acta* 58:797–810
- Wijbrans CH, Klemme S, Berndt J, Vollmer C (2015) Experimental determination of trace element partition coefficients between spinel and silicate melt: the influence of chemical composition and oxygen fugacity. *Contrib Miner Petrol* 169:1–33
- Wu C, Mason TO (1981) Thermopower measurement of cation distribution in magnetite. *J Am Ceram Soc* 64:520–522
- Zhukova I, O'Neill HSC, Cambell IH, Kilburn MR (2014) The effect of silica activity on the diffusion of Ni and Co in olivine. *Contrib Miner Petrol* 168:1029

**Publisher's Note** Springer Nature remains neutral with regard to jurisdictional claims in published maps and institutional affiliations.